Palaeogeography, Palaeoclimatology, Palaeoecology 634 (2024) 111953

Contents lists available at ScienceDirect

Palaeogeography, Palaeoclimatology, Palaeoecology

journal homepage: www.elsevier.com/locate/palaeo

Redox geochemical signatures in Mediterranean sapropels: Implications to constrain deoxygenation dynamics in deep-marine settings

Ricardo D. Monedero-Contreras [a,*], Francisca Martínez-Ruiz [a], Francisco J. Rodríguez-Tovar [b], Gert de Lange [c,d]

[a] Instituto Andaluz de Ciencias de la Tierra (CISC-UGR), Armilla, Spain
[b] Departmento de Estratigrafía y Paleontología, Universidad de Granada, Granada, Spain
[c] Utrecht University, Earth Sciences, Faculty of Geosciences, Utrecht, Netherlands
[d] Tongji University, Key Laboratory of Marine Geology, Shangai, China

ARTICLE INFO

Editor Name: Dr. Paul Hesse

Keywords:
Mediterranean
Sapropel
Deoxygenation
Paleoredox
Trace metal
Inorganic geochemistry

ABSTRACT

Global warming and anthropogenic activity are boosting marine deoxygenation in many regions around the globe. Deoxygenation is a critical ocean stressor with profound implications for marine ecosystems and biogeochemical cycles. Understanding the dynamics and evolution of past deoxygenation events can enhance our knowledge of present-day and future impacts of climate change and anthropogenic pressure on marine environments. Many studies have reconstructed the evolution redox conditions of past deoxygenation events using geochemical proxies. In this regard, the present work focuses on understanding the paleoenvironmental significance of geochemical redox signals derived from the onset, evolution and termination of regional-scale deoxygenations in deep-marine settings, with a specific focus on sapropels in the Eastern Mediterranean (EM). Sapropels, rhythmic organic-rich sediments deposited in EM, offer a unique opportunity to investigate recent deoxygenation events linked to past climate changes. Sapropels serve as paleo-archives of past deoxygenation events and can provide insights into the potential impacts of ongoing climate change on marine ecosystems and biogeochemical cycles. By integrating previous sapropel geochemical studies with a detailed analysis of new geochemical data from five Quaternary sapropels (S1, S5, S6, S7 and S8) in three different EM deep-marine settings, this study enhances our understanding of the paleoenvironmental significance of geochemical redox signals produced by deoxygenation dynamics and postdepositional processes in different deep-marine settings. The study supports that certain trace elements, such as Mo, V, U, Co, and Ni, are identified as more reliable redox proxies compared to Cr, Cu, Pb, and Zn. Four recurrent geochemical intervals attributed to specific redox conditions and postdepositional processes have been identified. Moreover, internal calibration of redox proxies thresholds has been performed and demonstrates how local environmental conditions (e.g., productivity rate) and hydrogeographic features (e.g., water-depth, particulate-shuttling intensity, deep-water renewal and fluvial input) play crucial roles in controlling the authigenic uptake rates of redox-sensitive trace metals, and subsequently, redox thresholds values of geochemical redox proxies. The results also emphasize the importance of postdepositional processes to accurately interpret geochemical signals in paleoenvironmental studies. This research enhances our overall understanding of geochemical signals associated with regional-scale deoxygenation events in deep-marine settings, offering new insights into predicting biogeochemical changes in marine environments undergoing a transition towards anoxia. By comprehending the dynamics of past and present deoxygenation, we acquire valuable knowledge regarding the potential effects of climate variability in marine ecosystems.

1. Introduction

Deoxygenation (reduction in oxygen levels) is an ocean stressor that alters biogeochemical cycles (e.g., C, N, P and trace metals) and with adverse effects on marine life (e.g., mass fish deaths). It is projected that deoxygenation will intensify in numerous marine regions worldwide by

* Corresponding author.
E-mail address: ricardo.monedero@csic.es (R.D. Monedero-Contreras).

https://doi.org/10.1016/j.palaeo.2023.111953
Received 1 August 2023; Received in revised form 18 September 2023; Accepted 28 November 2023
Available online 4 December 2023

the year 2100, making it an escalating concern for human society (Keeling et al., 2010; Schmidtko et al., 2017; Breitburg et al., 2018). Marine deoxygenation may arise in different marine settings as a result of (i) reduced water-column mixing due to increased surface-water temperature and freshening (Levin, 2018; Monedero-Contreras et al., 2023a), and (ii) the expansion of Oxygen Minimum Zones resulting from increased nutrients inputs in coastal areas that enhance marine productivity (Zirks et al., 2021). Past deoxygenation events have drastically shaped marine environments throughout Earth's history. These deoxygenation events tend to be recorded in deep-marine settings as organic-rich sediments (e.g., black shales) enriched in redox-sensitive trace metals (RSTMs), as occurred during (i) the Toarcian Oceanic Anoxic Events (T-OAEs) (Jenkyns, 1985; Hetzel et al., 2009; Dickson et al., 2017; Fernández-Martínez et al., 2023), (ii) the Paleocene-Eocene Thermal Maximum (PETM) (Schulte et al., 2013) or (iii) the Eocene-Oligocene transition; EOT) (Dickson et al., 2021). Paleoceanographic reconstructions of these past deoxygenation events enhance our understanding of deoxygenation dynamics and marine responses. In this regard, the study of past episodes of marine deoxygenation offers valuable paleo-perspectives to predict the potential impacts of deoxygenation on marine ecosystems and biogeochemical cycles derived from the current global warming and human-induced factors, such as nutrient pollution and habitat destruction (Hennekam et al., 2020; Mancini et al., 2023).

In general, black shales deposition occurred under very different Earth conditions and configuration than present. However, geologically "modern" analogs as the Eastern Mediterranean (EM) sapropels have recorded more recent regional-scale deoxygenation events (since the Miocene to the Holocene). These regional-scale deoxygenation events in EM can be considered as analogs for large-scale (i.e., global-scale) deoxygenation events (e.g., OAEs) since similar oceanographic processes are involved the Mediterranean and global ocean circulation (Giorgi and Lionello, 2008). In most cases, sapropel deoxygenation events are manifested in EM sedimentary record as rhythmic organic-rich sediment layers particularly enriched in trace metals (i.e., Mo, U, V, Cu, Co, Ba, etc.) (Cita et al., 1977; Kidd et al., 1978; Emeis et al., 1996, 2000; Warning and Brumsack, 2000; Gallego-Torres et al., 2007a; Rohling et al., 2015). The rhythmic deposition of sapropels in the EM is attributed to minimum astronomical precession cycles (orbital forcing) that promote cyclic periods of maximum insolation in the northern hemisphere. Consequently, African monsoons are intensified and forced to migrate northward, closer to the Mediterranean region (Lourens et al., 1996; Hennekam et al., 2014; Weldeab et al., 2014; Rohling et al., 2015). The intensified monsoons led to increased freshwater and nutrients inputs into the EM, which stimulated marine productivity. Simultaneously, these inputs slowed down or even stopped deep-water circulation. As a consequence, regional-scale deoxygenation occurred predominantly in bottom-waters, promoting the preservation of organic matter (OM) (Cita and Grignani, 1982; Rossignol-Strick, 1983, 1985; Casford et al., 2003; Gallego-Torres et al., 2007b, 2010; Marino et al., 2009; Rohling et al., 2015; Monedero-Contreras et al., 2023a).

Compared to older deoxygenation events, such as Paleozoic and Mesozoic Oceanic Anoxic Events (OAEs) recorded as black shales (Reershemius and Planavsky, 2021 and references therein), sapropels offer a better spatial and chronological control, and have been less affected by late diagenetic processes (Hennekam et al., 2020). Consequently, sapropels have been extensively used for paleoenvironmental and paleoclimatic reconstructions, providing paleo-perspectives that enhance our understanding of deoxygenation dynamics and environmental responses during climate variability. Many of these studies have provided paleoredox reconstructions based on geochemical proxies. However, despite extensive research, and the existing literature on sapropels geochemical signatures, still open questions remain. Particularly regarding the interpretation of redox geochemical signals in organic-rich sediments that derived from the interplay of deoxygenation dynamics and associated postdepositional processes in deep-marine settings.

Compiling and synthetizing the existing knowledge coupled with new data presentation and interpretation can offer new insights to further understand the environmental/oceanographic significance of geochemical signals in modern and paleo marine settings. In this regard, the individual contributions from previous sapropel geochemical studies have provided crucial insights for the recognition and interpretation of recurring geochemical intervals and boundaries in the sapropels layers and surrounding sediments (e.g., marker bed, oxidized interval, unoxidized interval, oxidation front and synsapropel interval). These intervals, as identified and elucidated by various studies, reflect variations in redox conditions and post-depositional processes. Notably, the marker bed, characterized by shifts from euxinic/anoxic to suboxic/oxic conditions, has been recognized and interpreted by the work of Thomson et al. (1995, 1999), de Lange (1986), Pruysers et al. (1991, 1993), Reitz et al. (2006) and others, highlighting the significance of Mn-oxyhydroxide precipitation and its association with trace metals after sapropel termination (Filippidi and de Lange, 2019). The oxidized interval, where RSTMs are depleted due to mineral host phase oxidation due to the downward migration of the oxidation front, is informed by Wilson et al. (1986), de Lange et al. (1989) and van Santvoort et al. (1996, 1997). Additionally, studies by Passier et al. (1996, 1997) have contributed to our understanding of the synsapropel interval, where pyrite enrichment occurs through the reaction of downward HS^- fluxes.

Within this context, this work focuses on unraveling the paleoenvironmental significance of geochemical redox signals derived from regional-scale deoxygenations in deep-marine settings. This is achieved by integrating the outcomes of past geochemical studies and a detailed analysis of new geochemical data obtained from five recent Quaternary sapropels (S1, S5, S6, S7, and S8) recovered at three EM deep-marine settings (Ionian Basin, Mediterranean Ridge and Eratosthenes Seamount). These sapropels were deposited under different degrees of bottom-water stagnation and oxygen-depletion. Consequently, the assessment of these five sapropels deposited in three different EM locations, allows to assess a wide spectrum of redox geochemical signals derived from diverse environmental and hydrogeographic conditions in different deep-marine settings. Furthermore, a calibration of redox proxies' thresholds has also been performed at each location using the approach proposed by Algeo and Li (2020). This calibration is crucial as it has been demonstrated that the authigenic enrichment rate of RSTMs is not only attributed to bottom-water redox conditions (Warning and Brumsack, 2000; Algeo and Li, 2020). Moreover, the collected data facilitated the reconstruction of the paleoenvironmental and paleoceanographic evolution of the five examined sapropels in EM.

The integrative approach of this study provides key insights and geochemical tools for the identification and subsequent interpretation of geochemical redox intervals in organic-rich sediments (e.g., black shales). This contributes to enhance the current understanding of geochemical signals produced by deoxygenation dynamics and associated postdepositional geochemical processes in deep-marine settings. Furthermore, valuable information can be obtained regarding potential biogeochemical changes that may arise in marine environments transitioning towards anoxic conditions. Consequently, this knowledge aids in evaluating strategies to mitigate the consequences of deoxygenation on vulnerable marine ecosystems.

2. Oceanographic setting

The Mediterranean Sea is a semi-enclosed and evaporative marginal sea connected to the Atlantic Ocean by the Strait of Gibraltar. Despite its limited size (~2,500,000 km^2), the Mediterranean Sea exhibits a strong thermohaline circulation and a complex system of currents capable of maintaining oxic and ultra-oligotrophic conditions in the water-column and sediments with low total organic carbon content (TOC) (Pinardi and Masetti, 2000; Millot and Taupier-Letage, 2005; Pinardi et al., 2015; Rohling et al., 2015). The unique characteristics of the Mediterranean

Sea make it highly sensitive to external forcing (e.g., astronomical oscillation, climate changes and anthropogenic pressure) and one of the most vulnerable regions to global climate change (Giorgi, 2006). Consequently, global climate variability and its consequences are manifested earlier in the Mediterranean Sea than in the global ocean (Lionello et al., 2006; Turco et al., 2015). Therefore, the Mediterranean Sea serves as an exceptional natural laboratory for studying the responses of marine environments to the current climate change, while its sedimentary record allows to study the nature and development of regional deoxygenation associated to past climate changes (Hennekam et al., 2020).

Atlantic Water enters the Western Mediterranean through the Strait of Gibraltar, where it undergoes modifications, resulting in a water mass with higher salinity and temperature known as Modified Atlantic Water (MAW). MAW enters EM through the Strait of Sicily (Fig. 1), where it keeps flowing eastward. As it flows to the Levantine Basin, MAW experience increases in salinity. During winter cooling, high evaporation rates caused by strong winds with dry air masses promote vertical mixing and the formation of Levantine Intermediate Water (LIW; between ~150 and ~ 600 m water-depth), which is then separated from the overlying MAW. The formation of Easter Mediterranean Deep Water (EMDW) primarily occurs in the Adriatic Sea by vertical mixing during strong winter winds from Europe, however, surface-water sinking at the Aegean Sea also contribute (Wüst, 1961; Miller, 1963; Lascaratos et al., 1999; Millot, 1999, 2009; Millot and Taupier-Letage, 2005; Rohling et al., 2015).

The five assessed sapropels (S1, S5, S6, S7 and S8), were sample in cores recovered from three ODP Leg 160 sites (964, 966 and 969). The sites describe an east-west transect across the EM and represent different deep-water regimes and water-depths. Site 964 is located at the Ionian abyssal plain and represents the deepest site (water-depth: 3658 m). This site is most influenced by the Adriatic Deep Water and Western Mediterranean water masses that come through Otranto Strait and Sicily Strait (Fig. 1), respectively. Site 969 is situated at the Mediterranean Ridge and west to the Levantine Basin at a water-depth of 2200 m and represents the centermost location of the EM (Fig. 1). Site 966 is the easternmost location, situated on the top of a pelagic high called Eratosthenes Seamount and the closest to the Nile River mouth. Site 966 represents the shallowest site at a water-depth of 940 m and is situated in the interface between LIW and EMDW.

3. Sapropel deposition

During sapropel deposition, circulation patterns and water masses dynamics were markedly different (Rohling et al., 2015; Andersen et al., 2020). Increased fresh-water discharge (mainly from the Nile River), due to monsoon intensification, weakened the anti-estuarine circulation, which resulted in decreased surface-water salinity and reduced vertical mixing (Gallego-Torres et al., 2007a; Tachikawa et al., 2015; Monedero-Contreras et al., 2023a). Increasing freshwater input led to enhanced nutrient input and marine productivity, and also to the formation of a strong halocline and restriction of deep-waters. In this situation, when deep-waters are not strongly restricted (intermittently ventilated), the redoxcline is normally located at the sediment-water interface (SWI), causing the porewater to become anoxic with euxinic confined microenvironments, even is sulfate is saturated (Martínez-Ruiz et al., 2000; Scott and Lyons, 2012; Tribovillard et al., 2008; Filippidi and de Lange, 2019). However, during strong water-column stratification, an upward migration of the redox chemocline (also known as the redoxcline) from below the SWI to the water-column can occur, allowing bottom-waters to reach anoxic or even euxinic conditions (Gallego-Torres et al., 2007a, 2010; Filippidi and de Lange, 2019; Benkovitz et al., 2020; Sweere et al., 2021).

During sapropels deposition, EM deep settings experienced varying degrees of bottom-water deoxygenation as a response to different oceanographic and climatic conditions (Monedero-Contreras et al., 2023a). Regarding the assessed sapropels, S1, S5 and S7 where deposited during interglacial periods, while S6 and S8 were deposited during glacial periods (Ziegler et al., 2010; Grant et al., 2016). However, sapropels S5 and S7 experienced the most intense bottom-water deoxygenation, followed by S6, S8 and S1, respectively (Gallego-Torres et al., 2007a; Wu et al., 2016, 2018; Sweere et al., 2021). The diverse sapropel scenarios derived in different degrees of OM preservation and rate of authigenic RSMTs uptake by seafloor sediments. The distribution and concentration of RSTMs and OM in sapropels have been used as geochemical signals to delimit the different sapropel deposition stages (i.e., pre-sapropel, onset, evolution, termination and early diagenesis) and evoke specific oceanographic processes and postdepositional disturbances, such as particulate-shuttling intensity, bottom-water reventilation and postdepositional oxidation and sulfidisation (Passier et al., 1996; van Santvoort et al., 1996; Reitz et al., 2006; Jilbert et al., 2010).

4. Materials and methods

4.1. Core description, sampling and chronology

Background sediment of the analyzed records is mainly composed by nannofossil clay, with minor variations in clay content, displaying colors ranging from brownish to greenish and grayish (Emeis et al., 1996). Characteristic layers, such as foraminiferal sandy levels, discrete tephra layers and rhythmic dark layers (i.e., the sapropels), are intercalated into the background sediments (Emeis et al., 1996, 2000). Slump and tephra layers were visually and geochemically identified.

Sampling at 2 cm resolution includes the underlying and overlying intervals of sapropels S1, S5, S6, S7 and S8. Sapropels S3 (85.8–80.8 ka) and S4 (107.8–101.8 ka) exist in EM sedimentary record but were not the focus of this study (Fig. 1c) (Grant et al., 2016). The onset and termination times of the selected sapropels are well established by previous studies: S1: 6.1–10.5 ka (MIS 1), S5: 121.5–128.3 ka (MIS 5e), S6: 165.5–178.5 ka (MIS 6d), S7: 191.9–198.5 ka (MIS 7a), and S8: 209.5–224.1 ka (MIS 7c-7d) (Fig. 1c) (Ziegler et al., 2010; Grant et al., 2016). Top and base boundaries of sapropel events were delimited using Ba/Al ratio profiles (a productivity proxy, see Section 3.4) (Murat and Got, 1987; de Lange et al., 2008; Gallego-Torres et al., 2010; Rohling et al., 2015).

4.2. Geochemical analysis

For all geochemical analyses, dried sediment samples were powdered in an agata mortar. Due to sample size limitations, major elements quantification by XRF was only performed in sapropel S1 from Site 964 (Ionian Basin). In this case, sediment samples were prepared as fused beads. XRF analyses were done at Instituto Andaluz de Ciencias de la Tierra (IACT), with a S4 Pioneer from BRUKER, equipped with 4 kW wavelength dispersive X-ray fluorescence spectrometer (WDXRF) of BRUKER spectrometer and a Rh anode X-ray tube (60 kV, 150 mA). For major elements quantification, XRF precision was better than ±0.3%. In the rest of samples, major elements were measured with an ICP-OES Perkin-Elmer Optima 8300 (Dual View) with an autosampler Perkin-Elmer. Certified standards (BR-N, GH, DR-N, UB-N, AGV—N, MAG-1, GS-N, and GA) were measured for element quantification. Trace elements, in all samples, were measured using an ICP-MS NexION 300d (Perkin Elmer) spectrometer using Rh as internal standard. For major elements, ICP-OES precision was better than ±1% and for trace elements ICP-MS precision was better than ±5% for analyte concentrations of 10 ppm (Bea, 1996).

Both ICP-MS and ICP-OES were performed at the Scientific Instrumentation Center (CIC) of University of Granada. They both measured the same solutions, which were prepared in batches of 25 to 30 samples. Analytical blanks were introduced in each sample batch. Solutions were prepared with 0,1 g of powdered sample in Teflon vessels, where successive acid digestions using HNO_3 (ultra-pure with a 69%

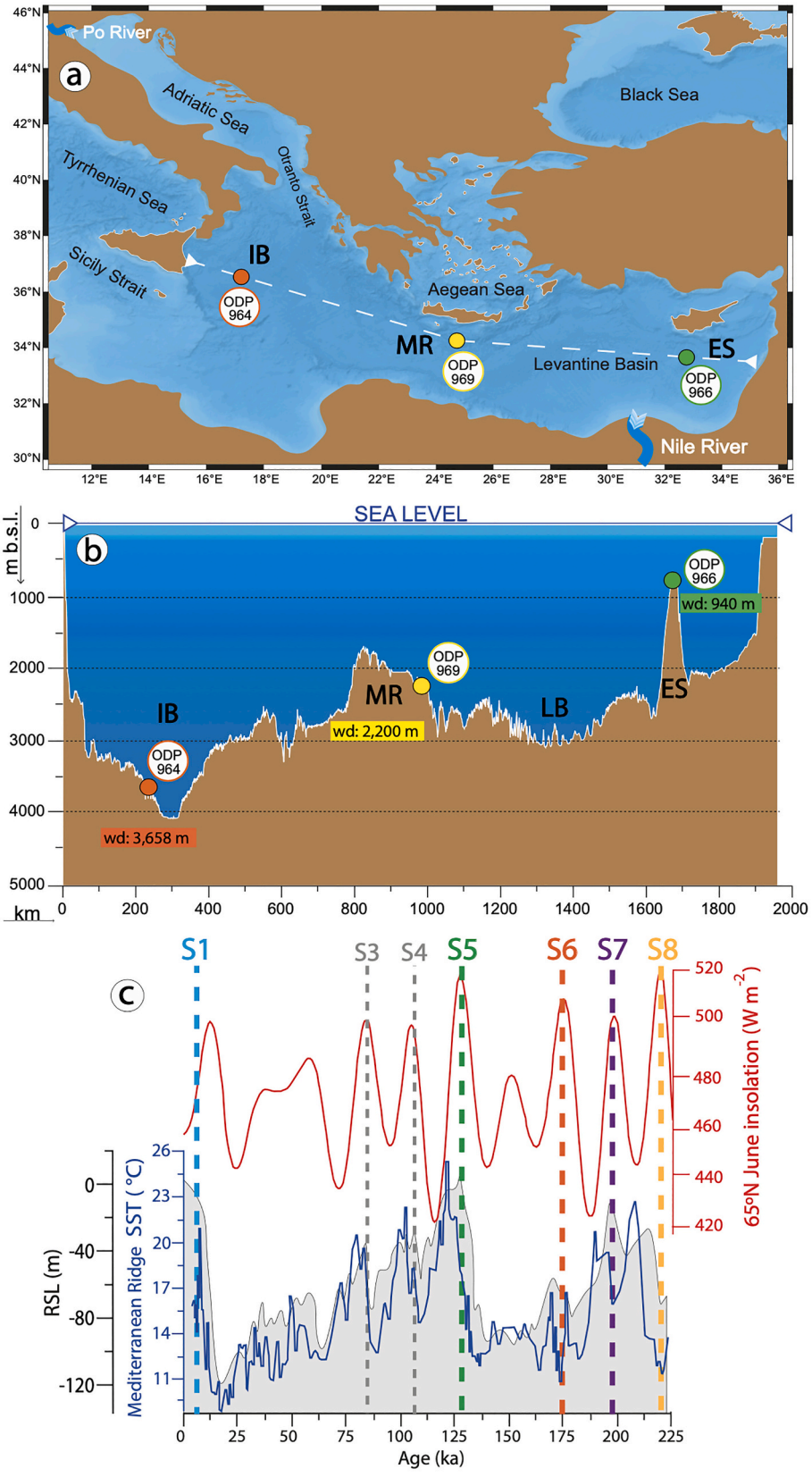

Fig. 1. (a) Map showing the location of the three studied ODP sites (964, 966 and 969) and water-depths (wd). IB: Ionian Basin, MR: Mediterranean Ridge, ES: Eratosthenes Seamount. (b) Bathymetry of the transect. (c) Temperature curve (SST, blue) at the Mediterranean Ridge (core M40–4/71), obtained from U^{K}_{37} by Emeis et al. (2003). Summer insolation (red) at 65°N from Laskar et al. (1993). Relative sea-level (RSL; light gray) from Grant et al. (2014). Sapropels under assessment are indicated with different colors that will be maintained henceforth in the following figs. (2-column fitting image). (For interpretation of the references to colour in this figure legend, the reader is referred to the web version of this article.)

concentration) and HF (48% concentration) were performed at 130 °C until evaporation. A final acid digestion with HNO_3 and water at 80 °C for 1 h was performed until samples were completely dissolved. Subsequently, the digested samples were diluted with Milli-Q water in 100 ml volumetric flasks following standard procedures (Bea, 1996).

Total organic carbon content, expressed as TOC%, was measured in ~50 mg of powdered samples by the Rock-Eval pyrolysis method at the Institute of Earth Sciences (ISTE) of the University of Lausanne. The Rock-Eval pyrolysis method consisted of a programmed temperature heating (from 200 °C to 850 °C, in successive steps), in a pyrolysis oven with an inert atmosphere (N_2). TOC% is calculated from the obtained thermograms using the following equation; TOC% = Pyrolyzed Carbon

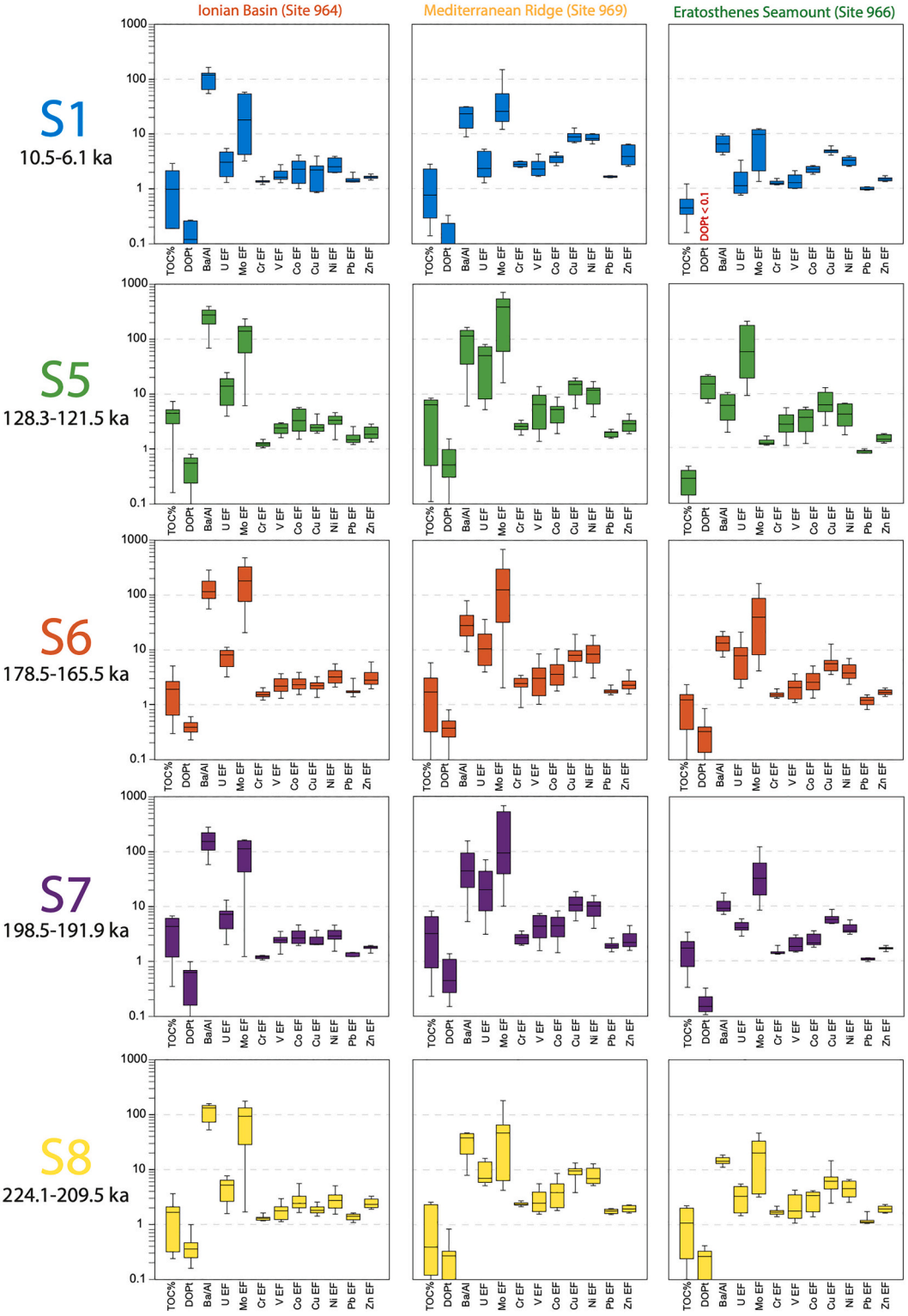

Fig. 2. Box-plots showing redox and productivity proxies values in sapropel intervals delimited by Ba enrichment, at the three locations: Ionian Basin (Site 964), Mediterranean Ridge (Site 969) and Eratosthenes Seamount (Site 966). Ba concentrations are expressed as Ba/Al (ppm/%) and RSTMs as EFs. (Single-column fitting figure).

(wt%) + Residual Carbon (wt%). Samples were calibrated using the IFP160000 standard with an instrumental precision of <0.1 wt% for TOC (Lafargue et al., 1998; Behar et al., 2001; Ordoñez et al., 2019).

4.3. Geochemical data normalization

Due to the conservative behavior of Aluminum, diverse studies support that Al-normalized trace metals (TM/Al) and trace metal Enrichment Factors (EFs) are the optimal normalization methods to evaluate trace metal variability and serve as reliable paleoenvironmental proxies (Brumsack, 2006; Tribovillard et al., 2006; Calvert and Pedersen, 2007; Algeo and Tribovillard, 2009; Algeo and Li, 2020; Algeo and Liu, 2020). Trace metals Enrichment Factors were obtained by applying the following equation: $TM_{EF} = (TM/Al)_{sample}/(TM/Al)_{reference}$, with the post-Archean Australian shale (PAAS) values from Taylor and McLennan (1995) as reference values to enable comparability with other studies, even if local background TM/Al values may be preferred over bibliographic reference values (Paul et al., 2023).

Vertical plots of environmental proxies allow to see variations in depth, delimit sapropels and stablish geochemical intervals within the sapropels and surrounding sediments (Figs. 4, 5 and 6). On the other hand, cross-plots offer information about geochemical differences between the established geochemical intervals within the sapropels and surrounding sediments. The variables introduced in the cross-plots (i.e., Mo/Al-Mn/Al, Ba/Al-TOC% and DOPt-TOC%) were selected to evidence differences and anomalies in geochemical intervals. Mo/Al-Mn/Al cross-plots (Fig. 7) evidence how some marker beds and synsapropel intervals the Mn-oxyhydroxides are enriched in Mo. RTSMs. Ba/Al-TOC% cross-plots (Fig. 8) enable the observation and determination of oxidized intervals, which show high Ba/Al values but low TOC% values. Moreover, it enables to assess the correlation between barite content and preserved OM in the different geochemical intervals. DOPt-TOC% cross-plots (Fig. 9) allow the observation of sapropels that developed synsapropel intervals, characterized by high DOPt values, but low TOC%. Consequently, cross-plots are an excellent tool to visually assess differences between geochemical intervals and sapropels. See section 5.1 for detailed information about geochemical intervals in sapropels.

4.4. Paleoenvironmental geochemical proxies

Diverse authigenic minerals precipitate during oxygen deficient conditions in marine systems, which enriched marine sediments in redox sensitive trace metals (i.e., Mo, U, V, Re, Cu, Co, Ni, Cr, Cu, Zn, Pb, Mn). Once normalized they can be used as redox proxies to determine different redox conditions in ancient marine environments (Figs. 2, 4–6) (Berner, 1981; Tyson and Pearson, 1991; Calvert and Pedersen, 1993, 2007; Crusius et al., 1996; Warning and Brumsack, 2000; Tribovillard et al., 2006; Scheiderich et al., 2010; Little et al., 2015).

Diverse geochemical proxies based on trace metal concentrations have been used to identify paleoredox changes in EM bottom-waters during sapropel deposition and to recognize geochemical intervals that reflect specific conditions and processes that occurred during deoxygenation and early diagenesis. Used redox proxies are: Fe/Al, Mn/Al, U_{EF}, Mo_{EF}, V_{EF}, Ni_{EF}, Cu_{EF}, Cr_{EF}, Co_{EF}, Zn_{EF}, Pb_{EF}, and degree of pyritization ($DOP_T = S_T * (55.85/64.12) / Fe_T$), where S_T = total sulfur, Fe_T = total iron and 55.85/64.12 represents weight ratios of Fe/S in stoichiometric pyrite (Berner, 1970; Algeo and Li, 2020). Therefore, DOPt values reflect pyrite content in the sediments. Preestablished DOPt redox threshold values (e.g., DOPt >0.45 = euxinic bottom-water; Scott and Lyons, 2012) are not applied since the value of this threshold can vary depending on the hydrographic conditions of each marine setting (Algeo and Li, 2020).

Other geochemical proxies complemented additional paleoenvironmental information (e.g., productivity and climate variability). Ba/Al ratio and TOC% were used to determine productivity changes in sapropel intervals. Ba/Al ratio increases in marine sediments are associated to higher barite ($BaSO_4$) abundance. Barite precipitation in the water-column has been linked to periods of increased productivity and OM degradation, principally in the mesopelagic zone (Dehairs et al., 1987; Bishop, 1988; Paytan et al., 2002, 2004; Paytan and Griffith, 2007). Therefore, Ba/Al is a well-accepted qualitative proxy for paleoproductivity and have been successfully applied to sapropels (Passier et al., 1999; Arnaboldi and Meyers, 2007; Gallego-Torres et al., 2007a, 2010; Martínez-Ruiz et al., 2000; Hennekam et al., 2014; Filippidi and de Lange, 2019; Benkovitz et al., 2020).

Aeolian inputs in marine sediments can be tracked using geochemical proxies for gran-size, such as Zr/Al. Zr occurs in marine sediments primarily as zircon ($ZrSiO_4$), which is principally transported to the ocean by wind. K is mainly in association with clay minerals (e.g., illite) that are transported to the ocean by the rivers (Calvert and Pedersen, 2007 and references therein). Consequently, Zr/Al and K/Al were used to reconstruct aeolian and fluvial input respectively, which can offer information about climate variability. In the EM during dry periods, large aeolian inputs from the Sahara-Sahel region occurred. Conversely, during wet and warm climates (as occurs in most sapropel events), large fluvial inputs, mainly from African borderlands, are registered (Bout-Roumazeilles et al., 2013; Rohling et al., 2015; Wu et al., 2016, 2018). Nevertheless, it has been proven that European borderlands also play an important role in EM during sapropels deposited during glacial periods, such as S6 (Gallego-Torres et al., 2007a).

4.5. Multivariant statistical analyses

Multivariant statistical analyses (e.g., correlation matrixes and Principal Component Analysis, PCA) of the geochemical data are used to achieve a deeper understanding of the geochemical data and sediment composition of the three EM sites. Subsequently, a better interpretation of geochemical redox signals. Correlation matrixes have been obtained using the software "PAST 4.0" from Hammer et al. (2001). Mayor elements, trace metals and other variables that were considered the most important for this paleoenvironmental study (i.e., Al, Mg, Ca, Sr, K, Zr, Ti, Mo, U, V, Cu, Cr, Co, Ni, Pb, Zn, Mn, Fe, Ba DOPt, and TOC%), were introduced into the correlation matrix. A p-value of (p) $\leq$ 0.01 was proposed as threshold to verify whether the established correlations were statistically significant or not. The correlations established in the correlation matrix of each location determined the variables introduced in the PCA.

PCA allowed the establishment of the principal geochemical affinities and fractions in each EM location. PCA was also performed with the software "PAST 4.0" from Hammer et al. (2001). Only variables that reached a moderate to strong correlation (correlation coefficient (r) between ±0.4 and ± 1) in the correlation matrix were introduced in the PCA to reduce statistical noise. It is important to highlight that both multivariant statistical analyses (i.e., correlation matrix and PCA), were performed using non-normalized elements so there are no pre-induced correlations that could mask the real affinities and associations of the variables under assessment.

4.6. Redox thresholds calibration

Every depositional unit has specific depositional, geochemical, environmental and hydrographic features that control trace metal uptake rate by seafloor sediments (Algeo and Lyons, 2006; Algeo et al., 2007; Algeo and Tribovillard, 2009; Tribovillard et al., 2012; Sweere et al., 2016; Scholz et al., 2017; Scholz, 2018; McArthur, 2019; Algeo and Liu, 2020). The interplay of specific depositional features in a marine basin determines the redox thresholds values of the redox proxies (Algeo and Li, 2020). Therefore, applying redox thresholds values calibrated for a specific geological formation to another geological formation or depositional unit, is an inaccurate approach according to Algeo and Li (2020). These authors proposed that, if possible, redox thresholds should be calibrated for each paleodepositional unit. In the case of the

present study, redox thresholds calibration was performed to the three EM sites to evaluate variations in RSTMs authigenic enrichment threshold and rate. It is important to note that postdepositional processes can affect the original concentration and position (i.e., depth) of RSTM and lead to inaccurate thresholds values calibration. For this reason, a prior assessment of the geochemical data is necessary to identify altered geochemical intervals and exclude them in the calibration cross-plots.

The "Compound covariant-sequential enrichment" approach optimized by Algeo and Li (2020) was applied to different redox proxies for the calibration of redox thresholds values. V_{EF}, U_{EF} and Mo_{EF} were used as calibrants, since the ionic couple reaction of V, U and Mo occur at a specific but different redox potential (p*e*) (Fig. 11a). Mo, U, and V are reduced from specific oxyanions (e.g., MoO_4^{2-}, $UO_2(CO_3)_3^{4-}$, and $H_2VO_4^-$) into stable solid phase species at specific low-oxygen conditions (Crusius et al., 1996). Therefore, V, U and Mo enrichments in oxygen-depleted sediments represent a precise redox threshold according to their position in the redox ladder (Grundl et al., 2011; Algeo and Li, 2020). In order to specify positions in the redox ladder and respective redox thresholds, we employed the terminology proposed by Algeo and Li (2020) and Algeo and Liu (2020). Within this context, V enrichment is used to obtain the suboxidized-subreduced threshold value (T1). U enrichment is used to obtain the dysoxic-anoxic threshold value (T2), which indicates if ferruginous condition were reached. While Mo_{EF} is used to obtain the anoxic-euxinic redox threshold value (T3) (Fig. 11a). Calibration of redox thresholds is only possible when the plotted redox proxies show a sequential enrichment and not a constant linear coenrichment. See Algeo and Li (2020) for detailed information about this calibration approach. Furthermore, the redox threshold values enable a qualitative comparison of RSTMs authigenic enrichments rates across different marine settings, offering valuable insights into the local dynamics of RSTMs in the water-column and porewater.

5. Results

5.1. Geochemical data

A comparison between the three EM locations reveals that Mo, U and V reach the highest concentrations at the Ionian Basin (Site 964), followed by the Mediterranean Ridge (Site 969). While the lowest concentrations occur at the Eratosthenes Seamount (Site 966). Mo is the RSTM with the highest enrichment of all at the three locations. Cr, Co, Cu, Ni, Pb Zn and Mn, which also correspond to RSTMs, are systematically more enriched at the Mediterranean Ridge, followed by the Eratosthenes Seamount and the Ionian Basin. Ba is most enriched in Mediterranean Ridge sediments. Conversely, Ba is least enriched in Eratosthenes Seamount sediments. TOC% and DOPt tend to be similar at the Ionian Basin and Mediterranean Ridge, but higher than at Eratosthenes Seamount. See Fig. 2 and Table S1 in Supplementary Material (Sup. Mat.) for detailed results.

Regarding the sapropel layers, a comparison between sapropel values reveal that S5 and S7 are the sapropels most enriched in trace metals and have higher concentration in pyrite (i.e., higher DOPt values). S6 sediments show strong enrichment in Mo, like S5 and S7. However, S6 exhibits more unstable trends of redox and productivity proxies in the vertical plots than the rest of sapropels at the three locations (Fig. 6). S1 and S8 register lower enrichments in trace metals, and DOPt than the rest of sapropels (S5, S6, S7), being S1 the sapropel with the lowest values (Fig. 2 and Table S1). Interestingly, even though S1 sediments show the lowest enrichments in most variables, is the most enriched sapropel in Mn, specially at Mediterranean Ridge (Fig. 4). S1 and S8 also exhibit the lowest TOC% values (below 1.5% mean), followed by S6 (below 2% mean). Therefore, S5 and S7 show the highest TOC% values, but are systematically higher in S5 sediments (Fig. 2 and Table S1). No evident signs of Ba remobilization or barite reprecipitation (e.g., Ba marked peak above or below organic-rich sediments) have been recognized in the studied sapropel, enabling the use of Ba/Al as a paleoproductivity proxy (van Os and Middelburg, 1991: Martínez-Ruiz et al., 2000). See vertical plots of environmental proxies for variations in depth (Figs. 4, 5 and 6) and cross-plots for differences in geochemical intervals (Figs. 7, 8 and 9).

5.2. Multivariate statistical analyses

The correlation matrixes and the PC1 vs. PC2 scatterplots elucidated geochemical affinities and allowed the establishment of four statistical groups (GRPs), which represent the main geochemical fractions in each EM location. For detailed information about the Correlation Matrixes and PCA results, see Sup. Mat. The four geochemical fractions are:

1) Terrigenous geochemical fraction (GRP1; red in Fig. 3). Also named the detritic fraction, is principally constituted by elements enriched in minerals mainly supplied by rivers and wind, e.g., Al, K, Rb, Ti and Zr (Calvert and Pedersen, 2007). Pb and Cr are considered RSTMs that can precipitate in association with authigenic sulfides during oxygen depletion (Tribovillard et al., 2006). However, our data suggests that these two elements are mainly enriched in the terrigenous fraction at the three locations. Consequently, its respective EFs should not be used as reliable redox proxies. Mg is an element that is mainly supplied by continental runoff in detritic and clay minerals (Calvert and Pedersen, 2007 and references there in). However, the Ionian Basin is the only location where Mg is mainly in association with the fluvial fraction. Conversely, at Eratosthenes Seamount and Mediterranean Ridge, Mg is isolated from the rest of the geochemical fractions. This may indicate that Mg, in these two locations, is incorporated in other sediment fractions and minerals, such as in authigenic Mg-rich carbonates. Interestingly, at Eratosthenes Seamount the fluvial fraction (Al, Ti, K and Rb; Fig. 3c), is better correlated than in the other two locations, probably due to its proximity to the Nile River mouth.
2) Authigenic geochemical fraction (GRP2; purple in Fig. 3). This geochemical fraction is enriched during sapropel deposition. Is composed by elements that are strongly enriched in authigenic minerals (e.g., sulfides and sulfates) or in organometallic compounds than precipitate under oxygen deficient conditions and high marine productivity. Consequently, this fraction is mainly enriched during sapropel deposition. The elements that conformed this fraction can be divided in: (i) chalcophile and siderophile elements (e.g., Mo, S, Ni, Cu, Co, and Zn). These elements tend to be scavenged from the water-column to the seafloor by Mn and Fe oxyhydroxides and OM (Tribovillard et al., 2006; Scholz et al., 2013). Once in seafloor and in the presence of dissolved H_2S produced by sulfate-reducing bacteria, they are fixed in association with pyrite (FeS), as demonstrates the robust correlation with DOPt, or by forming their own sulfides (e.g., MoS, CuS, CuS_2, NiS and [Zn,Fe]S CoS, NiS). (ii) Elements that are enriched in association with OM and occur in seawater in at least two oxidation states and precipitate as the less soluble lower oxidation state during oxygen depleted conditions (e.g., U and V) (Helz et al., 1996; McManus et al., 2005). (iii) Elements that precipitate in authigenic minerals due to intense OM degradation in the water-column during periods of increased marine productivity, such as Ba in barite ($BaSO_4$; see Section 4.4) (Bishop, 1988; Calvert and Pedersen, 2007; Paytan and Griffith, 2007; Martínez-Ruiz et al., 2018, 2019, 2020).
3) Mixed geochemical fraction (GPR3; magenta in Fig. 3). Constituted by RSTMs that are under strong detritic influence, as shown by the PCA. Due to local factors this geochemical fraction varies at each location according to the influence of the detritic fraction on the authigenic enrichment of RSTMs. At the Ionian Basin, this geochemical fraction is only represented by Cu and Fe (Fig. 3a), suggesting that these two elements are the RSTMs most influenced by the detritic fraction. In Eratosthenes Seamount sediments, the PCA

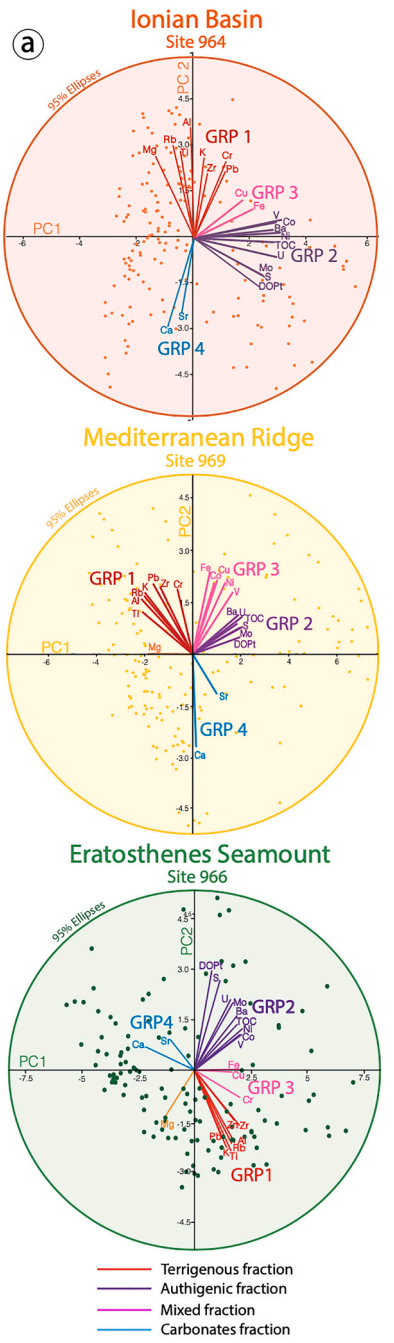

b

	Ionian Basin	Mediterranean Ridge	Eratosthenes Seamount
Variance% PC1	33.73	45.86	50.29
Variance% PC2	26.68	20.89	20.88
Variance% PC3	10.2	9.09	6.93
Variance% (PC1+PC2+PC3)	70.61	75.84	78.1
KMO	0.75	0.84	0.86

Fig. 3. (a) Scatter plots using PCA (x = PC1; y = PC2) of geochemical data from each location: Ionian Basin, Mediterranean Ridge and Eratosthenes Seamount obtained using PAST 4.0 (Hammer et al., 2001). (b) PCA statical values obtained at each location. The Kaiser-Meyer-Olkin Test (KMO) is a statistical test that measures adequacy of the data for factor analysis. Values closer to 1, indicate better adequacy. Mn was not included in the PCA of Site 966, and Zn and Mn were not included in the PCA of Site 964 and Site 969, since they did not present relevant correlation with the rest of the variables in the correlation matrices. See Sup. Mat. for detailed data. (2-column fitting figure).

suggests that Cr and Zn are also strongly influenced by the detritic fraction. While at the Mediterranean Ridge, the detritic fraction influences more RSTMs (e.g., Fe, Cu, Co, Ni and V; Fig. 3a). V is an element that tends to be enriched in association with humic and fulvic acids (i.e., OM) and normally is minimally influenced by the terrigenous fraction (Tribovillard et al., 2006). However, at the Mediterranean Ridge, V enrichments seem to be highly influenced by the detritic fraction. This could be linked to stronger particulate-shuttling and RSTMs scavenging at the Mediterranean Ridge.

4) Carbonates geochemical fraction (GRP4; blue in Fig. 3). Is constituted by Ca and Sr, which are characteristic elements of carbonate minerals, principally enriched under oxic conditions in the water-column and low productivity rates, i.e., during "non-sapropel" deposition.

6. Discussion

Geochemical records from EM sapropels have been exhaustedly studied. They represent exceptional paleo-archives for understanding regional oceanographic responses to past climatic changes (Hennekam et al., 2020; Mancini et al., 2023). Many of these studies have used variations in authigenic minerals (e.g., pyrite and barite), TOC and RSTMs distribution in the sapropel organic-rich sediments and surrounding sediments as geochemical signals for reconstruction of the environmental and physicochemical conditions in both the water-column and porewater during its deposition and early diagenesis (Passier et al., 1996; van Santvoort et al., 1996; Martínez-Ruiz et al., 2000; Reitz et al., 2006; Monedero-Contreras et al., 2023b).

6.1. Characterization of distinctive geochemical intervals in sapropel layers

Previous geochemical studies of sapropels, combined with a detailed analysis of new geochemical data obtained from five different sapropels (S1, S5, S6, S7 and S8) across three EM locations, have facilitated the recognition of recurring, yet distinct, geochemical patterns in sapropels and surrounding sediments, as previously explained in the introduction. Subsequently, these recurrent geochemical intervals and boundaries (i.e., marker bed, oxidized interval, oxidation front, unoxidized interval and synsapropel interval) have been interpreted in terms of redox conditions and postdepositional processes. However, it is important to acknowledge that these intervals are not uniformly present in all sapropels due to variations in environmental conditions and post-depositional processes.

- *Marker bed.* This geochemical interval is produced when the export of OM decreases and bottom-waters are reventilated, changing the redox regime in bottom-waters from euxinic/anoxic to suboxic/oxic (Fig. 12). Bottom-water ventilation causes oxidant downward fluxes (e.g., O_2 and NO_3) to exceed reductant upward fluxes (e.g., Fe^{2+}, Mn^{2+} and NH_4) in the porewater system (Thomson et al., 1993; de Lange, 1986). This in turns oxidizes OM and sulfides (enriched in trace metals) in the sapropel layer, and releases trace metals into porewaters (e.g., Mo, Cu, Co and Ni) that can precipitate above the organic-rich sediments in association with Mn-oxyhydroxides (Berrang and Grill, 1974; Pruysers et al., 1991, 1993; van Os and Middelburg, 1991; van Os, 1993; Thomson et al., 1995, 1999; van Santvoort et al., 1997; Tribovillard et al., 2006; Reitz et al., 2006). Consequently, during the termination of oxygen-depleted condition and intense reventilation (as occurred during sapropel termination), large quantities of Mn-oxyhydroxides precipitate on the top of the organic-rich sediments and be recognized by a marked Mn/Al peak (Filippidi and de Lange, 2019). This feature was also reported by de Lange (1986) in turbidites sequences at the Nares Abyssal Plain (western North Atlantic).

The Mn/Al peak is sometimes accompanied by an increase in other trace metals, principally Mo, Co, Cu, Ni and to a lesser extent Pb, Cr and Zn (Fig. 7). These elements precipitated in association with Mn-oxyhydroxides under suboxic conditions (during reventilation) and not as metal-organic ligands or in association with iron sulfides under euxinic conditions as there are no co-enrichments with DOPt, U, V or TOC in this interval (Figs. 5, 8 and 9). In some sapropel layers, several of these trace metals (Mo, Co, Cu and Ni) present in their vertical profiles a "double-peak" pattern and in some exceptional cases a "triple-peak" pattern, as occurs with Mo and Cu in S1 at the Mediterranean Ridge. In the latter mentioned case, each peak is associated to a different geochemical interval (Fig. 4). A similar case was recently observed by Filippidi and de Lange (2019), where a Mo enrichment in association with Mn-oxyhydroxides is observed on the top of S1 (delimited by Ba enrichment) at the Otranto Strait sill. A Mn and Mo coenrichment was also observed by Calvert and Pedersen (1993) at the deep continental margin of Baja California between the oxic/suboxic boundary at ~10 cm below the SWI. Consequently, the recognition of these postdepositional Mo enrichments is essential for accurate paleoredox interpretations since it evidences that a Mo enrichment by itself does not necessary imply a strong oxygen depletion. Hence, it is recommended that Mo, serving as a redox proxy (e.g., Mo_{EF}, Mo/Al, Mo ppm) should be employed in conjunction with the Mn/Al ratio and other established redox proxies within a multiproxy approach framework to prevent

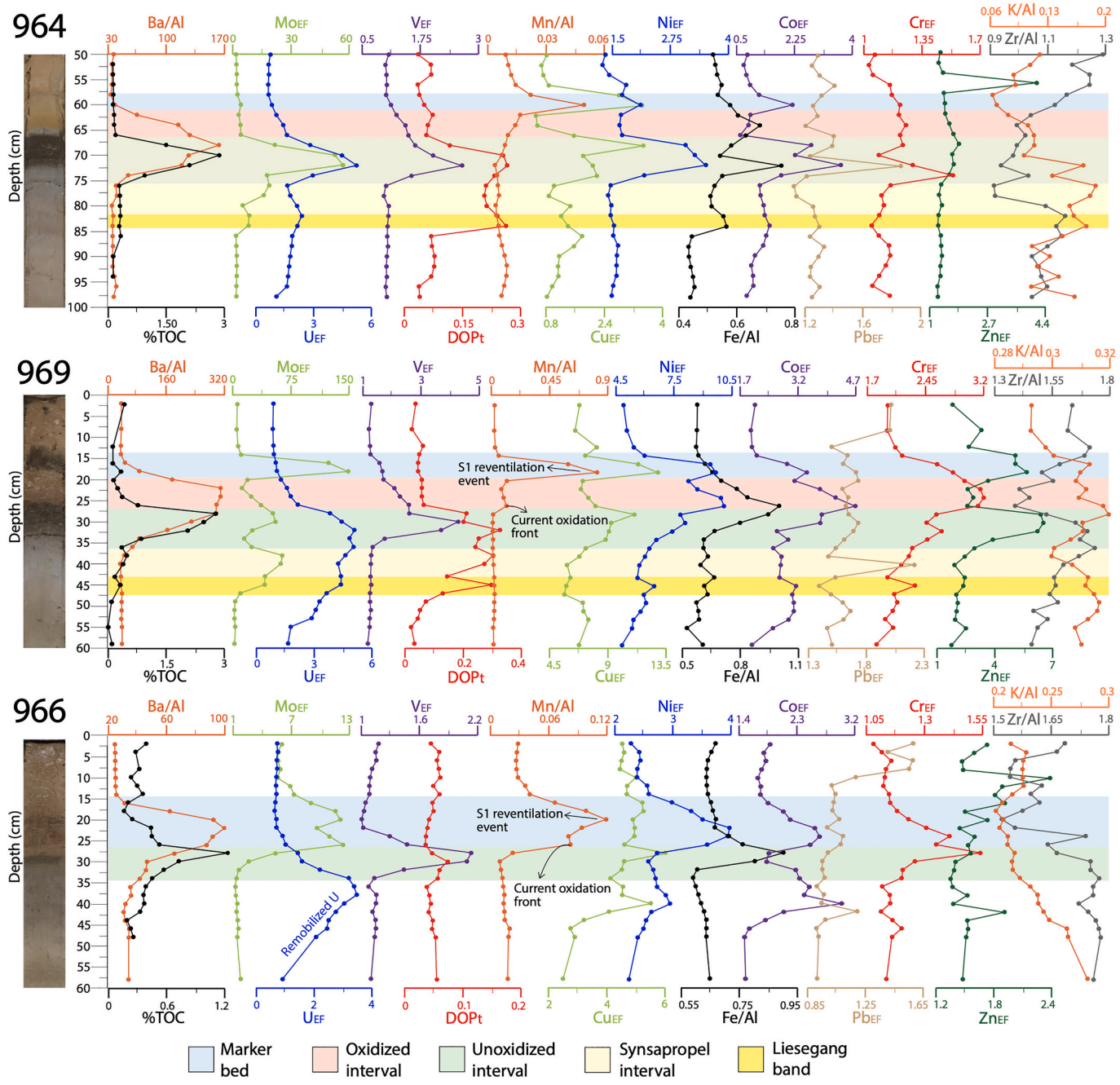

Fig. 4. Vertical plots of different redox, productivity and environmental proxies from sapropel S1 at the three EM sites: Ionian Basin (Site 964), Eratosthenes Seamount (Site 966) and Mediterranean Ridge (Site 969). Fe/Al and Mn/Al in %/%, while Ba/Al and Zr/Al in ppm/% ($x10^{-4}$). To simplify the figure and facilitate data interpretation, vertical plots of Cr/Al, Zn/Al and Pb/Al for S1 are presented in a separate Sup. Mat. figure, which includes all assessed TMs (Fig. S16). Geochemical redox intervals and sedimentary layers in the sapropels are illustrated in different colors. (Single-column fitting figure).

misinterpretations and explore diverse mechanisms contributing to RSTMs enrichment, extending beyond the singular influence of oxygen depletion (Algeo and Lyons, 2006; Algeo and Maynard, 2004; Tribovillard et al., 2006; Algeo and Tribovillard, 2009; Lyons et al., 2009).

- *Oxidized interval.* Trace metals are impoverished in this interval due to oxidation of their mineral host phases (e.g., sulfides or OM; Fig. 10) during downward migration of the oxidation front (Fig. 12) (Wilson et al., 1986; de Lange et al., 1989; Thomson et al., 1995; van Santvoort et al., 1996, 1997). Sulfide oxidation is evidenced by the abrupt decrease in pyrite content (i.e., DOPt) in this interval (Fig. 9).

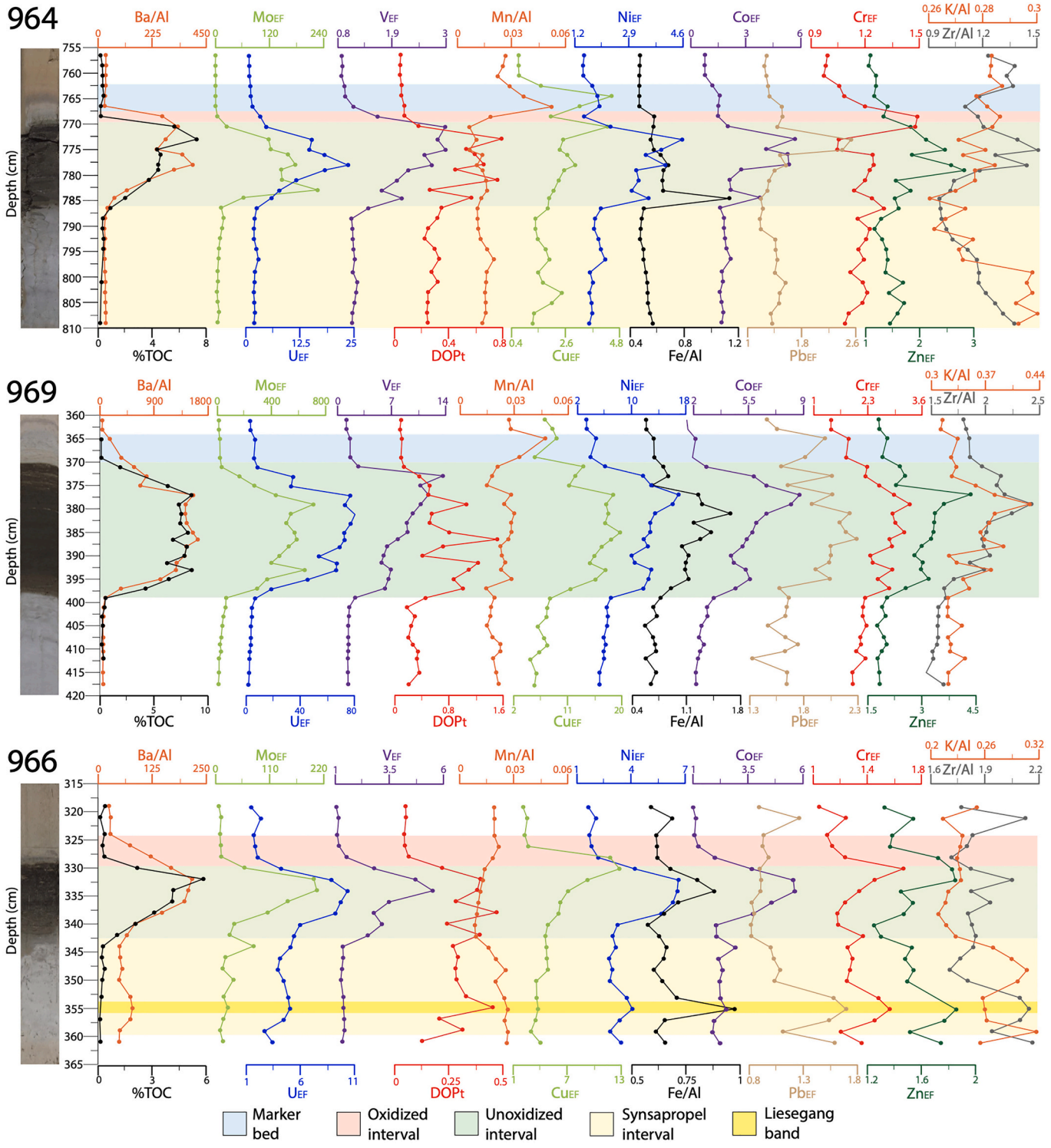

Fig. 5. Vertical plots of different redox, productivity and environmental proxies from sapropel S5 at the three EM sites: Ionian Basin (Site 964), Eratosthenes Seamount (Site 966) and Mediterranean Ridge (Site 969). Geochemical redox intervals and sedimentary layers present in the sapropel sequence are illustrated in different colors. To simplify the figure and facilitate data interpretation, vertical plots of Cr/Al, Zn/Al and Pb/Al for S5 are presented in a separate Sup. Mat. figure, which includes all assessed TMs (Fig. S17). Fe/Al and Mn/Al in %/%, while Ba/Al and Zr/Al in ppm/% (x10^{-4}). See Fig. 8 for legend. (Single-column fitting figure).

The lower boundary of this geochemical interval, which represents the oxidation front, is recognized by a mismatch between the two productivity proxies (i.e., Ba/Al and TOC%). In this oxidized interval, Ba/Al values continue high, while TOC% values decrease (Fig. 8) since OM is more susceptible to postdepositional oxidation than barite ($BaSO_4$), the main host mineral of Ba in sapropel sediments van Os and Middelburg, 1991; van Os, 1993; Nijenhuis et al., 1999; Martínez-Ruiz et al., 2000; Monedero-Contreras et al., 2023b). In this sense, the good preservation of biogenic barite in EM sediments have allowed the recognition of "ghost sapropels", which correspond to sapropel layers that have undergone total OM oxidation (Higgs et al., 1994; Wehausen and Brumsack, 2000).

The extent of the oxidized interval is closely related with bioturbation since it has been demonstrated that bioirrigation plays an important role in postdepositional oxidation of organic-rich sediments (Tribovillard et al., 2008; Löwemark et al., 2006). When deep-water circulation reactivates and oxic conditions returned to bottom-waters, opportunistic organisms (e.g., *Chondrites*-producers; recognized in sapropel layers Fig. S16 in Sup. Mat.) colonize the substrate and stimulate bioirrigation (Löwemark et al., 2006). This promotes (i) deeper and more efficient penetration of oxygenated water in the sediments and (ii) dissolution of mineral phases that host RSTMs (Figs. 10 and 12). Dissolved RSTMs diffuse from the oxidized interval back to the water-column and downward below the sapropel where they reprecipitate as anoxic/euxinic conditions still exist (Zheng et al., 2002; McManus et al., 2005; Tribovillard et al., 2006, 2008). Evidence of this postdepositional process is the isolated U enrichments below the organic-rich S1 sediments at the Mediterranean Ridge and Eratosthenes Seamount, where U (mainly hosted in association with OM) experienced downward migration and reprecipitation due to intense bioirrigation during bottom-water reventilation. (Fig. 4).

If bottom-water reventilation/reoxygenation occur progressively, passing from strong reducing conditions (euxinia/anoxia) to weak reducing conditions (dysoxia/suboxia), a preferential enrichment of V over U and Mo can occur on the top of the sapropel, as occurs on the top of S5 at the Ionian Basin (Fig. 5). This is based on the fact that V can precipitate in weak reducing conditions, where neither Mo nor U authigenic enrichment occurs (Tribovillard et al., 2006). However, in most cases, sapropel termination seems to occur abruptly, i.e., with a synchronous drop in RSTMs. Furthermore, if a slump or tephra layer is immediately deposited on the top of a sapropel layer, it can act as "redox shield" that prevents oxygenated water to efficiently reach the underlying organic-rich sediments (Filippidi et al., 2016). This probably occurred in sapropels where slumps and tephra layers where recognized (e.g., S6 at the Ionian Basin and the Mediterranean Ridge; Fig. 6).

- *Unoxidized interval.* This interval is characterized by the highest TOC and barite content in the sapropel sequence (Fig. 8), and by the high and coeval enrichment of RSTMs and DOPt. Furthermore, anoxic/euxinic porewater promote the dissolution of Mn-oxyhydroxides in this interval (see S5 at Site 966 and S7 at the three sites; Figs. 5 and 6) (Monedero-Contreras et al., 2023b). This is corroborated in the Mo/Al - Mn/Al cross-plots, where the data points belonging to the unoxidized interval tend to be impoverished in Mn (Fig. 7). However, the rest of RSTMs, mainly associated to iron sulfides, did not suffer evident postdepositional oxidation or dissolution (Fig. 10). Therefore, this geochemical interval is the most reliable for elucidating the syndepositional redox conditions during deoxygenation events and the most suitable for redox thresholds calibration. The high Mo concentrations in unoxidized sediments (over 200 ppm; Fig. 2), principally at the two deep-marine settings, can be explained by intense particulate-shuttling that enhanced Mo transfer from the water-column to the seafloor, where is liberated in porewaters as MoO_4^{2-}. The molybdate ion is transformed to thiomolybdates in the presence of free H_2S/HS^-, where is finally fixed in association with sulfides (Berrang and Grill, 1974; Crusius et al., 1996; Helz et al., 1996; Zheng et al., 2000; Morford et al., 2005; Scholz et al., 2013, 2017).

The correlative enrichment of DOPt and Fe with Mo, Cu, Co, Ni, Pb, and to a lesser extent with Zn and Cr in this geochemical interval, suggest that these RSTMs precipitated in association with iron sulfides (i.e., pyrite) or by forming their own sulfides, which only occurs in successive sulfidation reactions that require persistent sulfidic conditions in porewaters (Tribovillard et al., 2006). However, the PCA scatterplots show that in EM sediments Pb and Cr are strongly enriched in the detritic fraction. Accordingly, their enrichments in the unoxidized interval in sapropels characterized by large fluvial inputs from the Nile River such as S5 and S7 (Gallego-Torres et al., 2010; Wu et al., 2018), derive from the (i) increased detritic input and (ii) enhanced authigenic sulfides precipitation during euxinia.

Many sapropels in the unoxidized interval have linear regression coefficients over 0.65 ($r^2 \geq 0.65$) between Ba/Al and TOC%, emphasizing the good correlation and sometimes exceptional ($r^2 \geq 0.8$) between preserved OM and barite content (Fig. 8). This supports that (i) Ba enrichment in sapropel sediments is indeed related to biogenic barite (Martínez-Ruiz et al., 2000), and (ii) that the increased production of OM aggregates during sapropel deposition may have played a vital role in preserving pelagic barite crystals as they sink through the oxygen-depleted water-column, even in deep-EM settings, such as the Ionian Abyssal plain, where the prolonged transit time to the seafloor makes barite crystals more susceptible to dissolution (Light et al., 2023). Furthermore, the positive linear correlation of Ba and OM supports that barite content in sapropels have not been significantly affected by diagenetic dissolution during porewater euxinia since this would have resulted in an evident Ba impoverishment in respect to TOC (Paytan et al., 2004). Passier et al. (1997) reported $\delta\ ^{34}S$ pyrite values from −37.3‰ to −38.2‰ in S1 sapropel, indicating that SO_4^{2-} reduction took place in an open system with seawater exchange. Thus, the porewater sulfate-reduction did not lower sulfate concentrations enough for barite dissolution and remobilization of Ba (Martínez-Ruiz et al., 2000). The preservation of biogenic barite was also corroborated by SEM observations of barite crystals in different geochemical intervals of S1 (Fig. S15), including the unoxidized interval which was under permanent anoxic conditions. However, this is not the case in other organic-rich deposits derived from high carbon export and low bottom-water oxygen, where sulfate-reducing conditions in the bottom-water and porewater promoted the dissolution of barite crystals (McManus et al., 1994, 1998). Dissolved barium can reprecipitate as euhedral diagenetic barite at the sulfate methane transition zone (SMTZ), as occurs in Paleozoic organic-rich strata (Torres et al., 1996; Grema et al., 2022) or above the oxidation front as occurs in modern Black Sea sediments (Henkel et al., 2012).

- *Synsapropel interval.* According to the DOPt-TOC% cross-plots, DOPt verticals plots and SEM images, many sapropels have pyrite enrichments below the organic-rich sediments (Figs. 9 and 10). The precipitation of pyrite below some sapropels is controlled by the reaction of downward HS^- fluxes with the upward diffusing Fe from underlying sediments (Fig. 12) (Passier et al., 1996). Sulfate reducing bacteria degrade the OM in the overlying organic-rich sediments and produce HS^-. If reactive iron (Fe_{HR}) in the unoxidized interval is exhausted by the formation of iron sulfides (principally pyrite) and HS^- production by sulfate reducing bacteria is greater than the upward Fe^{2+} flux, the excess of HS^- will diffuse out of the sapropel (Fig. 10). The excess of HS^- can diffuse back to the water-column where it contributes to bottom-water euxinia or diffuse downwards below the organic-rich sediments, up to 20 cm below the unoxidized interval, where it promotes the precipitation of large pyrite framboids as large euhedral aggregates (>20 μm), principally into foraminifera chambers (Fig. 10a), producing the so called "synsapropel

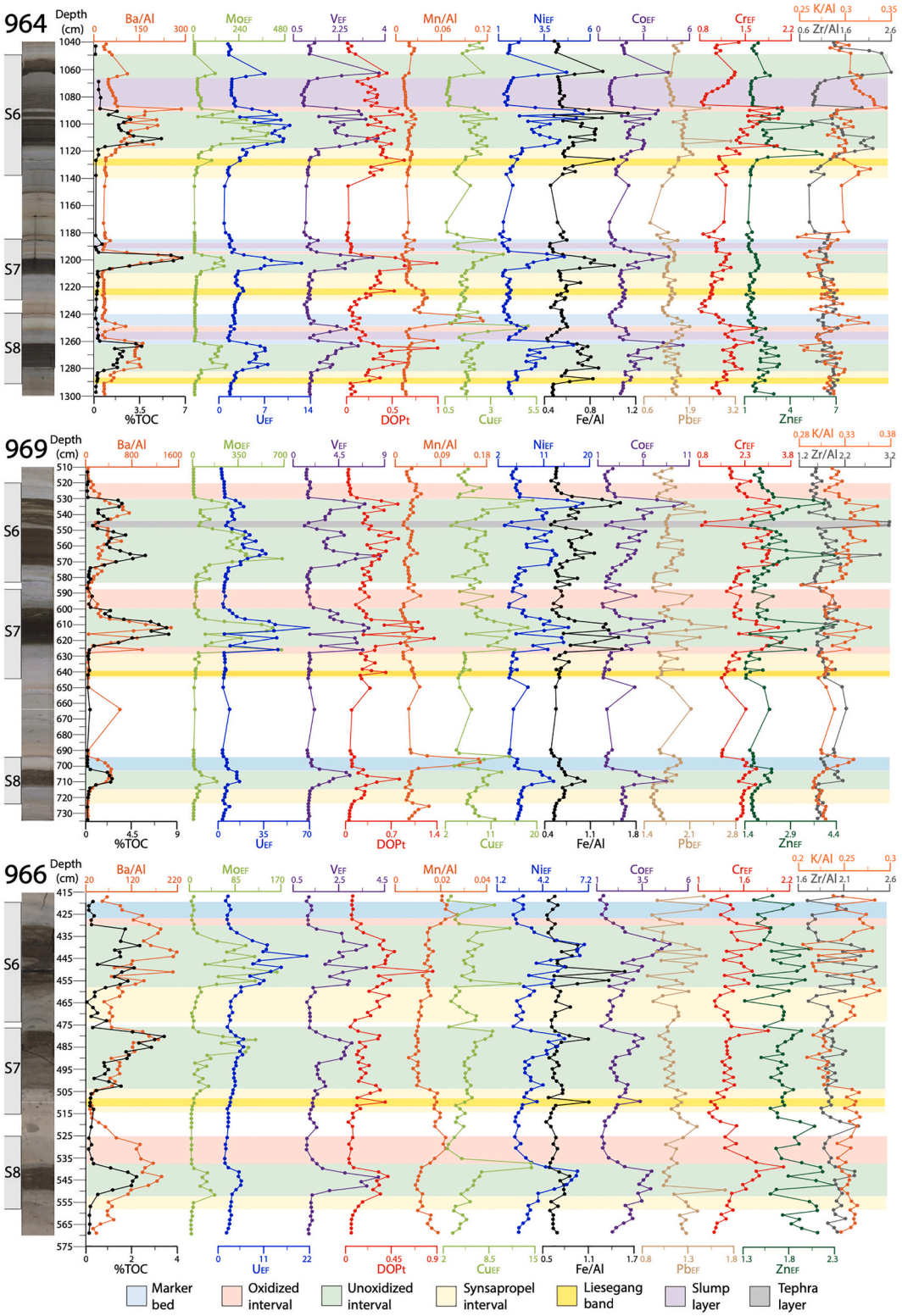

Fig. 6. Vertical plots of different redox, productivity and environmental proxies from sapropels S6, S7 and S8 at the three EM sites: Ionian Basin (Site 964), Eratosthenes Seamount (Site 966) and Mediterranean Ridge (Site 969). Geochemical redox intervals and sedimentary layers present in the sapropel succession are illustrated in different colors. To simplify the figure and facilitate data interpretation, vertical plots of Cr/Al, Zn/Al and Pb/Al for S6, S7 and S8 are presented in a separate Sup. Mat. figure, which includes all assessed TMs (Fig. S18). Fe/Al and Mn/Al in %/%, while Ba/Al and Zr/Al in ppm/% (x10^{-4}). See Fig. 8 for legend. (Single-column fitting figure).

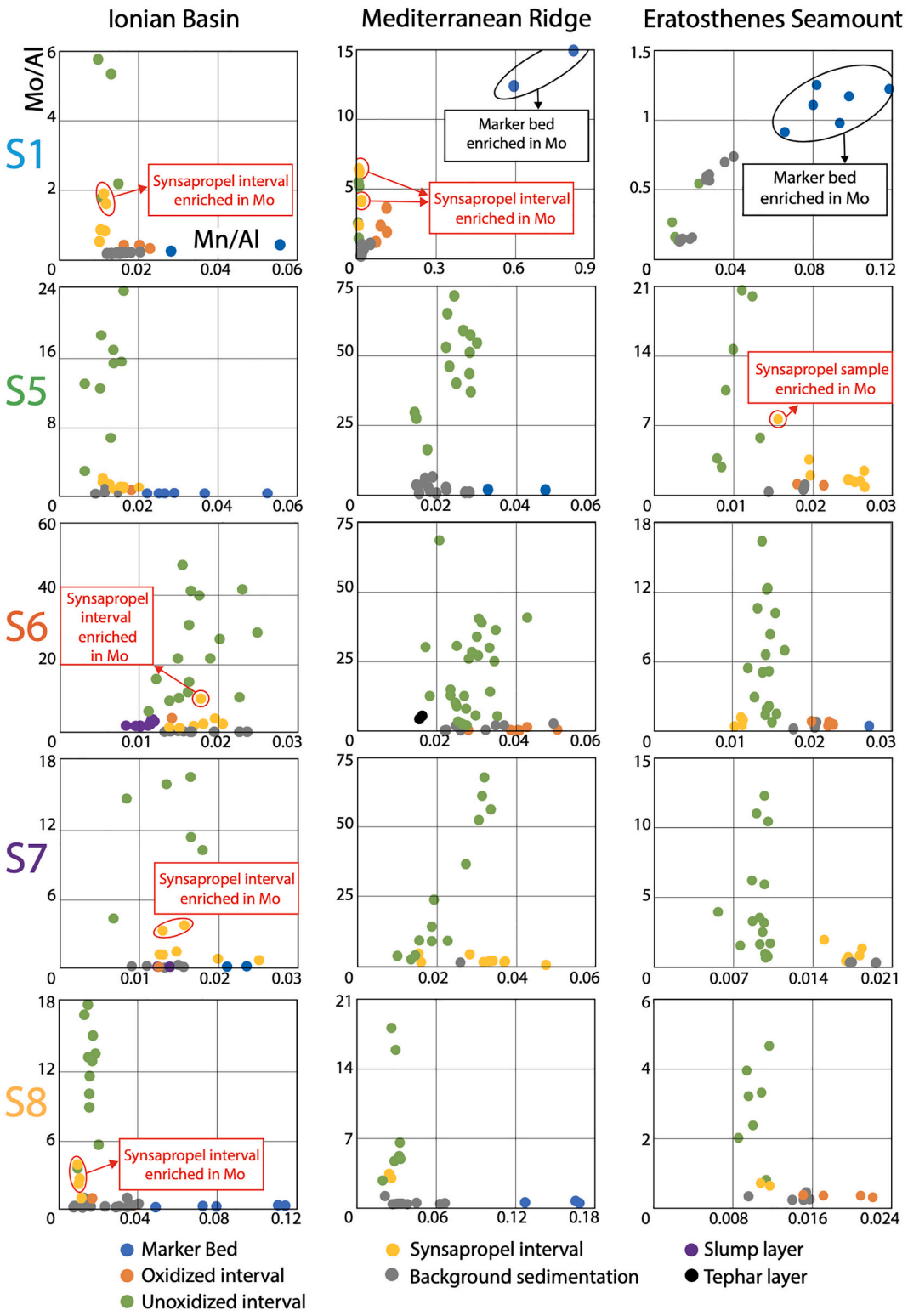

Fig. 7. (a) Mo/Al - Mn/Al cross-plots of sampled sapropels (S1, S5, S6, S7, S8) at the three EM locations. Redox geochemical intervals are illustrated with different colors. y-axis: Mo/Al, x-axis: Mn/Al. (Single-column fitting figure).

interval" (Berner, 1970; Passier et al., 1996, 1997; Zhang et al., 2014; Liu et al., 2019). The precipitation of large pyrite aggregates probably occurs in confined euxinic microenvironments or microniches, as the ones facilitated by the foraminifera shells (Tribovillard et al., 2008). Certain pyrite aggregates underwent the formation of euhedral regrowths displaying a distinct "sunflower" texture (Fig. 10a). Such textures are typically associated with late diagenesis processes (Lin et al., 2016; Chang et al., 2022). Similar pyrite textures have been observed at the paleo-SMTZ (submarine methane seepage zone) in select Paleozoic formations (Grema et al., 2022)

If a synsapropel interval is absent, as occurs in S8 at the Ionian Basin (Fig. 6), in S1 at Eratosthenes Seamount (Fig. 4) and in S5 at the Mediterranean Ridge (Fig. 5), we can infer that during its deposition and

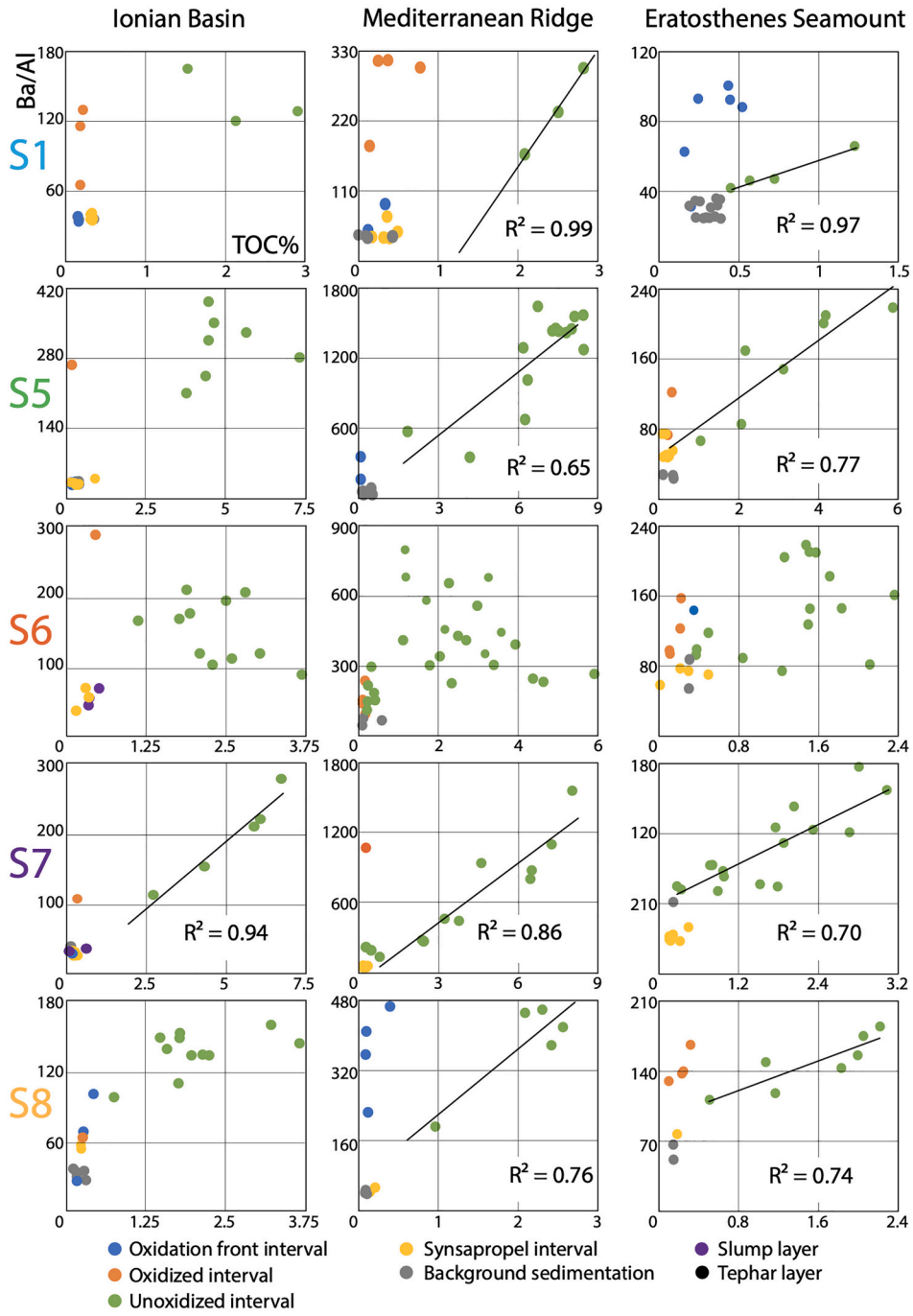

Fig. 8. Ba/Al (ppm/%; x10^{-4})-TOC% cross-plots of sampled sapropels (S1, S5, S6, S7, S8) at the three EM locations. Redox geochemical intervals are illustrated with different colors. Correlation coefficients (R^2) are shown in sapropels that have $R^2 > 0.6$. Dashed lines indicate the original TOC% prior to the oxidation according to the obtained correlation slope. y-axis: Ba/Al, x-axis: TOC%. (Single-column fitting figure).

early diagenesis, the production of HS^- by sulfate reducing bacteria never exceeded the sum of the upward Fe^{2+} flux and the Fe_{HR} pool in the organic-rich sediments (Fig. 10) (van Os and Middelburg, 1991; Passier et al., 1996, 1997). Therefore, a lack of synsapropel suggest that Fe_{HR} did not act as a limiting factor for pyrite precipitation and HS^- did not effectively diffuse out of the organic-rich sediments. Conversely, if a synsapropel interval exists, we can infer that: (i) Fe_{HR} acted as the limiting factor for pyrite precipitation in the organic-rich sediments, and (ii) HS^- downward diffusion exceeded the upward Fe^{2+} flux (Fig. 10b). In respect to the timing of the synsapropel interval formation, downward sulfidisation developed as soon as the HS^- production exceeded the Fe availability for pyrite formation within the sapropel. Therefore, the formation of the synsapropel interval occurred during sapropel deposition and not before as suggested by its relative position in the sedimentary record (Passier et al., 1997).

In sapropels that developed a synsapropel interval, two different situations can be distinguished according to the patterns observed in DOPt vertical profiles. In the first situation the system remains HS^- dominated and the DOPt profile in the synsapropel interval shows a broad increase, but with no marked DOPt peaks (e.g., S5 at the Ionian Basin and S6 at Eratosthenes Seamount; Figs. 5 and 6). In the second situation, at the lower boundary of a synsapropel interval, DOPt and Fe/Al profile exhibit a peak recognized in previous studies as "Liesegang band" (Berner, 1969; Passier et al., 1996; Bektursunova and L'Heureux,

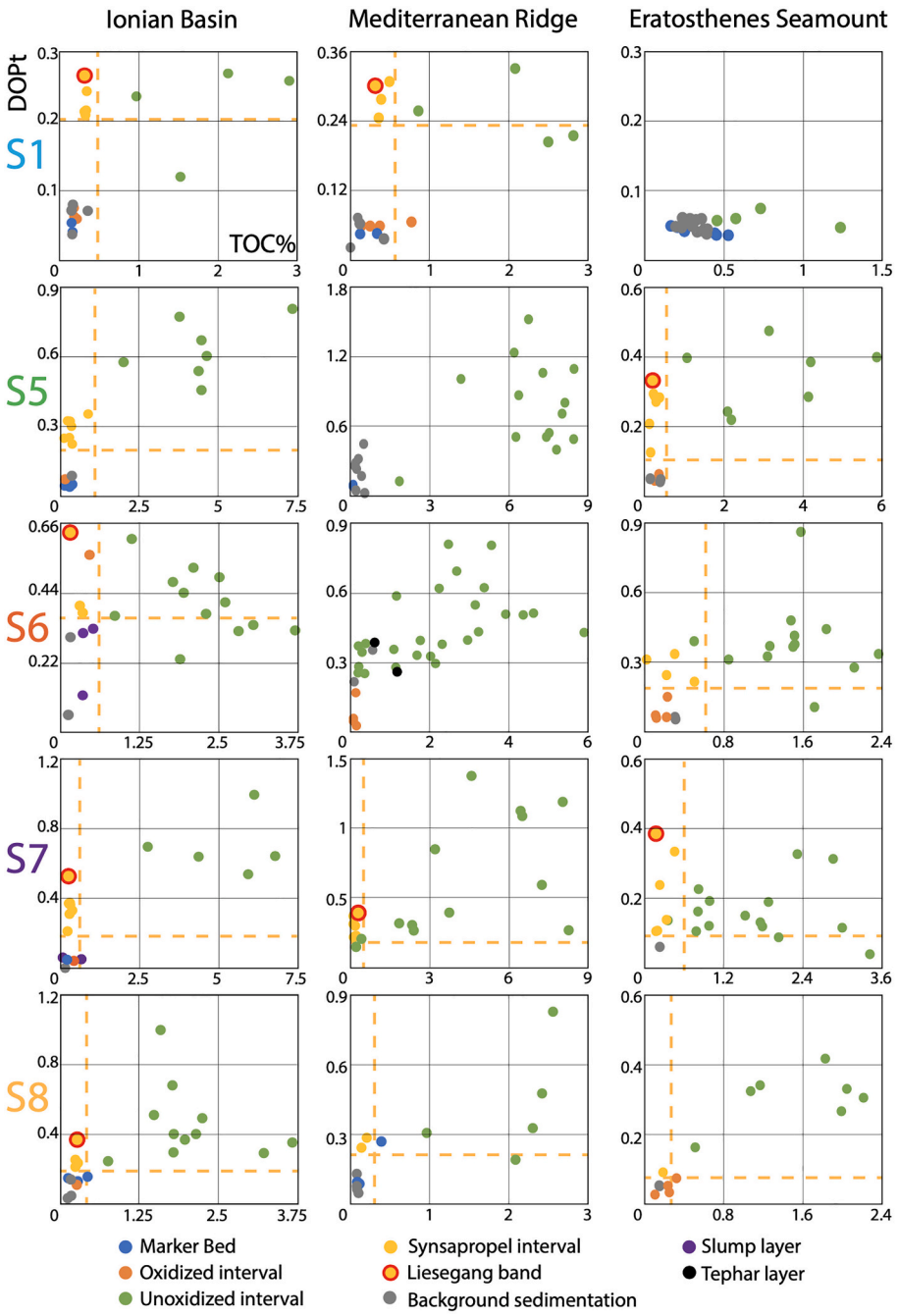

Fig. 9. DOPt-TOC% cross-plots of sampled sapropels (S1, S5, S6, S7, S8) at the three EM locations. Redox geochemical intervals are illustrated with different colors. Yellow dashed lines are shown to delimit the high DOPt and TOC% values associated to the unoxidized interval from the high DOPt values with low TOC% associated to the synsapropel interval. y-axis: DOPt, x-axis: TOC%. (Single-column fitting figure). (For interpretation of the references to colour in this figure legend, the reader is referred to the web version of this article.)

2011). In this band, DOPt can reach higher values than in the unoxidized interval, as occurs in S1, S6 and S7 at the Ionian Basin, in S5 and S7 at Eratosthenes Seamount and in S1 and S5 at the Mediterranean Ridge (Fig. 9) (Berner, 1970; Passier et al., 1996, 1997). The Liesegang band indicates the stratigraphic position where the downward HS^{-} flux was balanced with the upward Fe^{2+} flux diffusing from the dissolution of Fe-oxides in the underlying sediments (Fig. 10) (Berner, 1970; Passier et al., 1996, 1997).

Furthermore, the DOPt vertical plots indicate that Mo and to a lesser extent other RSTMs (e.g., Co, Cu, Ni, Cr, Zn and Pb) precipitated in association with iron sulfides in the synsapropel interval or were trapped by pyrite aggregates through surface absorption, creating in this way sub-mm RSTMs enrichments (Fig. 7). Mo is the most efficiently trapped RSTM by the pyrite aggregates during early diagenesis (Tribovillard et al., 2008; Monedero-Contreras et al., 2023b) also noted that. These enrichments are more marked in the Liesegang bands where pyrite precipitation is more intense and present large recrystallized euhedral crystals with "sunflower" texture (Merinero et al., 2017; Chang et al., 2022). These types of syndepositional enrichment of RSTMs below the organic-rich sediments occurred in S1 at the Ionian Basin and the Mediterranean Ridge and in S5 at Eratosthenes Seamount (Figs. 4 and 5), as also observed by Filippidi and de Lange (2019) in S1 in deep and intermediate EM settings.

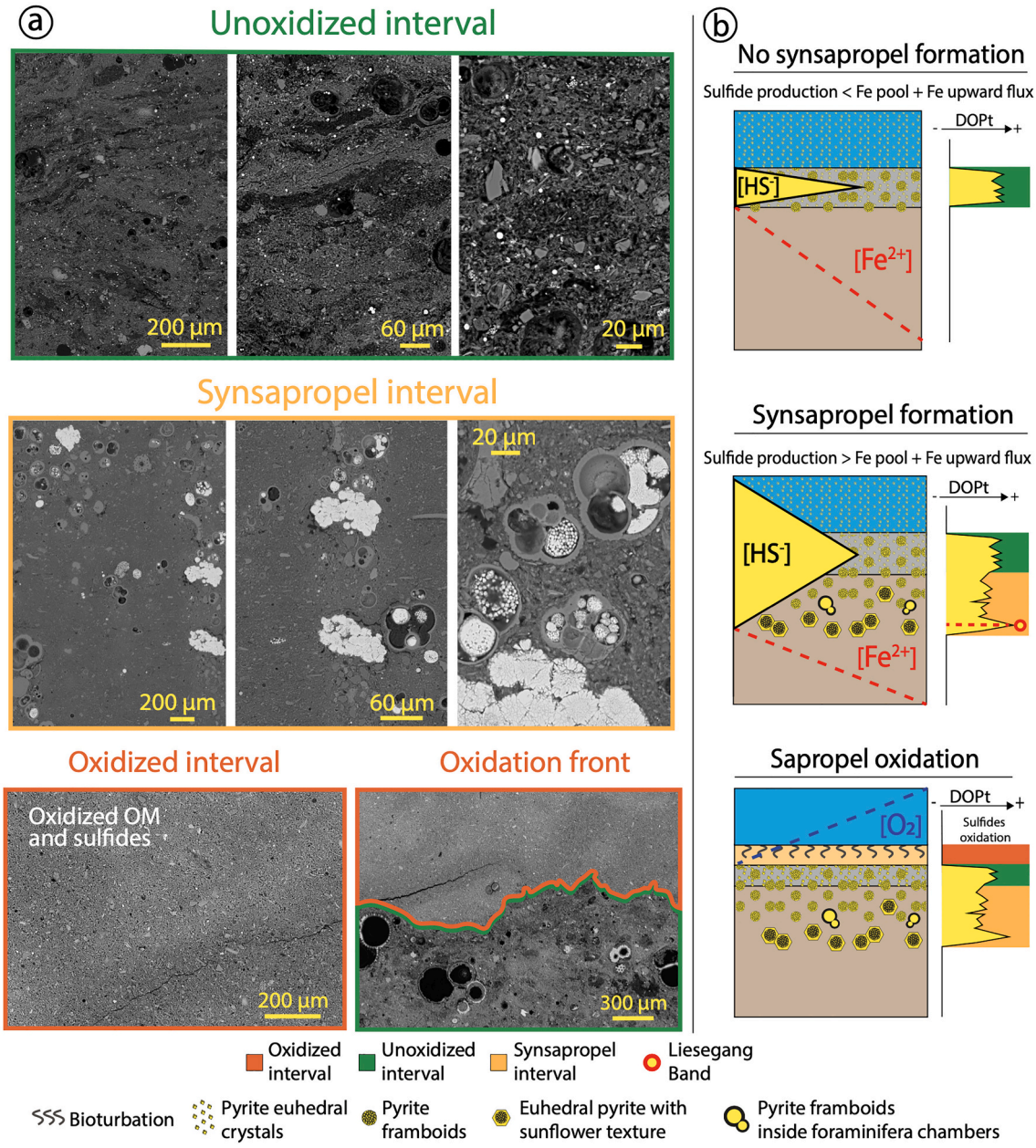

Fig. 10. Sample from sapropel S1 at the Ionian Basin (Site 964) (a) SEM images using backscattered electron detector (BSD) at different scales from different sapropel intervals (oxidized, unoxidized and synsapropel). Note that the oxidized interval shows no OM or pyrite crystals, the unoxidized sapropel interval shows small and scattered pyrite framboids and irregular OM laminae, and the synsapropel interval presents large pyrite framboids, principally inside foraminiferal shells, large euhedral pyrite crystals and no OM laminae. (b) Synsapropel formation scheme modified from Passier et al. (1997) showing expected DOPt signal (i) in subsaturated HS^- systems, (ii) in oversaturated HS^- system, and (iii) in oxidized sapropels. Different redox geochemical intervals are illustrated with different background colors in the simplified DOPt trends (green: unoxidized interval, dark yellow: synsapropel interval, orange: oxidized interval). (Single-column fitting figure). (For interpretation of the references to colour in this figure legend, the reader is referred to the web version of this article.)

6.2. Redox thresholds calibration

The establishment of geochemical intervals in sapropel layers allowed the recognition of altered samples due to postdepositional processes (e.g., oxidation, bioirrigation, downward sulfidisation, etc.) that have affected the syndepositional concentration of the RSTMs. As previously stated, during sapropel termination Mn-oxyhydroxides precipitate and absorb RSTMs, such as Mo, Co, Cu and Ni, which then creates TMs enrichments that are not associated to oxygen-depleted conditions (Tribovillard et al., 2008; Filippidi and de Lange, 2019). In this regard, only samples corresponding to the unoxidized interval were incorporated into the calibration plots, considering that this particular interval is less affected by postdepositional processes and preserved better the syndepositional enrichments of RSTMs. It is worth mentioning that Pb_{EF} and Cr_{EF} did not present a marked enrichment in the calibration plots at any location (see Sup. Mat.), inhibiting the calibration of the authigenic enrichment threshold. This is probably due to the fact that Pb and Cr enrichment in the unoxidized interval is not only in association with increased sulfides content, but also in association with increased detrital minerals content, as corroborated by the PCA geochemical fractions.

The calibrated redox proxies show identical values for all three redox thresholds (T1 = T2 = T3; Fig. 11b), making it impossible to calibrate them separately. As a result, the values obtained from T1 and T2

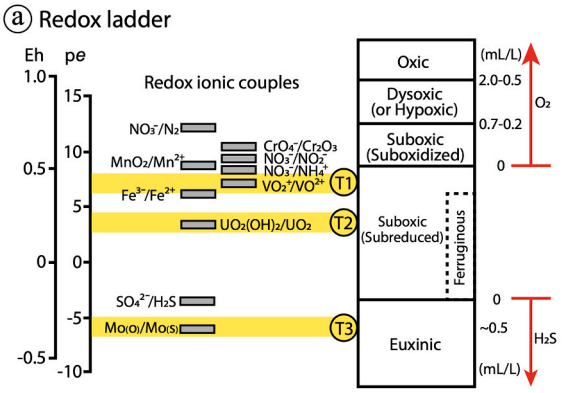

b Redox thresholds

Location	Threshold	UEF	VEF	CuEF	CoEF	NiEF	CrEF	DOPt
Ionian Basin	T1	-	-	*	1.7	2	1	0.1
	T2	-	*	1.3	1.7	2	1	0.1
	T3	3	1.3	1.3	1.7	2	1	0.15
Mediterranean Ridge	T1	-	-	8	*	7	2.3	0.5
	T2	-	*	8	6	7	2.3	0.5
	T3	5	*	8	6	7	2.5	0.5
Eratosthenes Seamount	T1	-	-	6	2	3	1.4	0.1
	T2	-	*	6	2	3	*	0.1
	T3	4	1.5	6	2	3.5	1.4	0.1

Fig. 11. (a) Modified redox ladder scheme from Algeo and Li (2020) and Algeo and Liu (2020). Redox potentials (Eh) and electron activities (p*e*) of redox ionic couples at pH 7 are presented in the redox ladder. The yellow fields (T1, T2 and T3) represent the redox thresholds. (b) Table showing the redox thresholds values for different redox proxies at the three studied sites. (*) denotes where simple covariation pattern (i.e., co-enrichment) impeded redox thresholds calibration. (Single-column fitting figure). (For interpretation of the references to colour in this figure legend, the reader is referred to the web version of this article.)

correspond to the T3 value, which represents the anoxic-euxinic threshold. This indicates abrupt redox transitions in EM deep-waters during sapropels onsets and terminations. Such abrupt redox transition towards anoxic/euxinic EM bottom-waters promoted a synchronous co-precipitation of V, U and Mo, while inhibiting a progressive and preferential enrichment of V and U over Mo (Algeo and Li, 2020). This finding goes in agreement with previous studies that state a rapid onset of oxygen-depleted conditions in deep and intermediate EM settings (de Lange et al., 2008; Azrieli-Tal et al., 2014; Tesi et al., 2017; Filippidi and de Lange, 2019; Andersen et al., 2020; Zirks et al., 2019, 2021). The abrupt establishment of euxinic conditions is further supported by the synchronic and abrupt co-enrichment of Mo with U, V and other RSTMs observed in the vertical plots (Figs. 4, 5 and 6) and by the linear covariation between Mo, U and V ($r^2 \geq 0.5$ and ≤ 0.8; see Sup. Mat.).

Comparing the redox threshold values obtained for each EM deep-marine setting enables to assess local hydrogeographic factors on RSTMs uptake/burial rates. Among the three locations, the Mediterranean Ridge consistently exhibits higher redox thresholds values, while the Ionian Basin exhibit the lowest values (Fig. 11; for detailed data see Sup. Mat.). This indicates that the background concentrations of RSTMs are higher in the Mediterranean Ridge sediments (Fig. 11b). Therefore, the authigenic enrichment of RSTMs due to euxinic conditions begins at lower concentrations in the Ionian Basin than in Eratosthenes Seamount and Mediterranean Ridge. Consequently, redox thresholds values differ between locations (Fig. 11b). Moreover, this might suggest that the Ionian Abyssal plain is more prone to develop sulfidic bottom-waters due to rapid onset of deep-water stagnation since the T3 threshold is crossed at lower RSTMs concentrations. The highest redox thresholds values are found at the Mediterranean Ridge and could be associated to more vigorous particulate-shuttling and efficient RSTMs scavenging. Enhanced particulate-shuttling boosts trace metal transfer from the water-column, as occurs in the modern Black Sea (Dellwig et al., 2010;

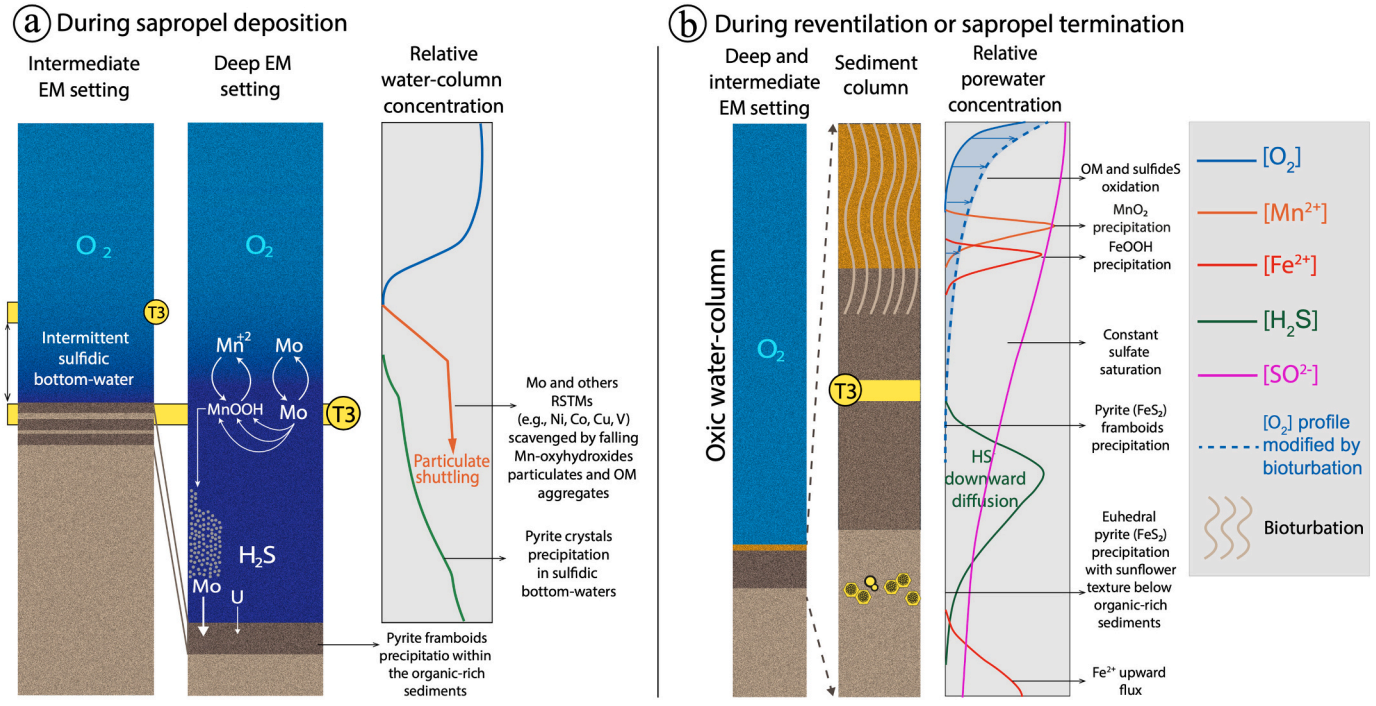

Fig. 12. Redox schemes based on Passier et al. (1996), Algeo and Tribovillard (2009) and Canfield and Thamdrup (2009), showing redox ions profiles: (a) during sapropel deposition in intermediate and deep-marine settings, and (b) during reventilation events or sapropel termination. Ion water-column profile for deep-marine settings is based on the modern Black Sea water-column chemical profile from Canfield and Thamdrup (2009). (Single-column fitting figure).

Algeo and Li, 2020). Therefore, intense particulate-shuttling promotes higher RSTMs concentrations in deep-marine sediments, and subsequently higher authigenic uptake rates. These findings go in accordance with Warning and Brumsack (2000) data, who also compared geochemical from different EM deep sites and stated that not only water-depths plays a key role on RSTMs authigenic enrichment, since they observed that EM sites with very different water-depths developed similar RSTMs enrichment. Moreover, our findings align with the Fernández-Martínez et al. (2023), who demonstrated that despite the global-scale impact of the T-OAE event, the local oceanographic and environmental features of each Toarcian basin were the main controls in the development of bottom-water euxinia.

While these redox thresholds values cannot be considered quantitative values, the observed variability among sites demonstrates that RSTMs concentration in marine sediments is not solely determined by bottom-water redox conditions and water-depth (Warning and Brumsack, 2000). Instead, RSTMs concentration can exhibit significant variations across oceanographic settings with equivalent redox conditions due to differences in particulate-shuttling intensity, bottom-water renewal frequency, fluvial input, and source material composition. This is supported in prior studies which conducted comparative analyses and empirical assessment of diverse anoxic to euxinic basins characterized by distinct oceanographic attributes, both in modern and ancient oceans, using geochemical cross-plots (e.g., U_{EF} - Mo_{EF} and RSTMs - TOC), to elucidate the main factors that control the enrichment of RSTMs in marine environments (Algeo and Lyons, 2006; Algeo and Maynard, 2004; Algeo and Tribovillard, 2009; Lyons et al., 2009; Algeo and Li, 2020; Algeo and Liu, 2020). Additionally, Tribovillard (2021), indicates that the geochemical properties of the sediment, such as availability of Fe_{HR} in the porewater and the rate of OM decomposition within sediments seem to also affect the authigenic enrichment rate of RSTMs, especially RSTMs that are strongly scavenged by OM, such as Ni and Cu. Overall, our results in conjunction with prior studies outline the importance of considering local hydrogeographic and environmental factors and geochemical properties of the sediments, since the interplay of these factors control the authigenic enrichment rate of TMs in organic-rich sediments that recorded past deoxygenation event, such as black shales or sapropels. This supports Algeo and Li (2020), who highlight the need for internal calibration for each individual depositional system in order to consider local variability and achieve more robust redox interpretations of RSTMs.

6.3. Paleoenvironmental analysis of sapropel events

A number of conclusions regarding the paleoceanographic and paleoenvironmental conditions that ruled each sapropel event can be pointed in the light of previous studies. According to the Mo enrichments, deep-marine settings in EM developed sulfidic porewaters during all sapropel events; however, not all of them developed perennial sulfidic bottom-waters. The stability of sulfidic bottom-waters is controlled by the intensity of surface water freshening and productivity rate (Monedero-Contreras et al., 2023a). In this sense, sapropels with intense surface water freshening due to strong African monsoons (e.g., S5 and S7) are the ones that developed the most perennial sulfidic bottom-waters (Wu et al., 2018; Sweere et al., 2021). This is corroborated in this study, where S5 and S7 show the strongest oxygen depletion and highest productivity rates among the five studied sapropels. Moreover, in S5 and S7 the marker bed is less evident and in some cases absent (Figs. 5 and 6), indicating weak postdepositional oxidation probably due to higher sedimentation rates (higher fluvial inputs) and less vigorous reventilation. However, during S7 deposition at the Mediterranean Ridge, two ventilation events seem to have occurred during its deposition, as suggested by two correlative decreases in RSTMs concentrations in S7 unoxidized interval at Eratosthenes Seamount and Mediterranean Ridge (Fig. 6).

Conversely, in sapropels associated to weaker African monsoons, such as sapropels S1 and S8, redox proxies in the unoxidized interval indicate weaker oxygen depletion than during S5, S6 and S7 due to weaker surface water freshening and lower productivity rates (Gallego-Torres et al., 2007a, 2007b; Rohling et al., 2015; Sweere et al., 2021; Monedero-Contreras et al., 2023a). However, vigorous and abrupt reventilation and oxygenation of bottom-waters during S1 and S8 termination is evidenced by abrupt marker beds (Figs. 4 and 6). In S1 layer at Eratosthenes Seamount (the shallowest setting), two Mn/Al peaks and associated Mo enrichments are observed (Fig. 4). The upper Mn/Al peak was produced during S1 termination by intense reventilation, while the lower Mn/Al peak is still diagenetically forming due to downward migration of the current oxidation front where dissolved upward diffusing Mn^{2+} from the underlying anoxic sediments is reprecipitating as Mn-oxyhydroxides (van Santvoort et al., 1996; Filippidi and de Lange, 2019). Regarding sapropel S8, intense reventilation during its termination is only registered in the two deepest sea settings (i.e., Ionian Basin and Mediterranean Ridge), but not at Eratosthenes Seamount (Fig. 6). This might occur because during S8, at Eratosthenes Seamount, bottom-waters were mainly under suboxic conditions, which did not allow intense Mn redox cycling in the overlying water-column and the subsequent massive precipitation of Mn-oxyhydroxides. However, intermittent and brief porewater euxinia at Eratosthenes Seamount needs to be evoked to explain the Mo enrichments in the unoxidized interval. This goes in agreement with Zirks et al. (2021) who state that intermediate EM settings during sapropels can develop bottom-water euxinia due to expansion of the Oxygen Minimum Zones.

S6 is an interesting sapropel since it was deposited during glacial period with lower sea-level. Its vertical plots present irregular and spiny trends (like a tooth-saw) in the redox and productivity proxies at the three locations. Key redox proxies (Mo_{EF}, U_{EF}, V_{EF} and DOPt) and productivity proxies (TOC% and Ba/Al) show correlative fluctuating trends within the unoxidized interval. Zr/Al and K/Al in S6 show abrupt changes in aeolian and fluvial input which indicates variable climatic conditions, which supported unstable hydrographic regime with strong productivity changes and redox fluctuations (Fig. 6). S6 is the sapropel that presents the highest Mo concentration at the three locations, even though it is not associated to the strongest deep-water deoxygenation (Gallego-Torres et al., 2007a; Sweere et al., 2021). This could be associated to a more intense particulate-shuttling and a fluctuating chemocline that promoted frequent Mo resupply to bottom-waters and "Mo burial pumps" as occurs in the modern restricted Cariaco Basin and Saanich Inlet (Jacobs et al., 1985; Crusius et al., 1996; Algeo and Tribovillard, 2009; Monedero-Contreras et al., 2023a).

7. Conclusions

This study highlights the importance of improving our understanding of geochemical signals derived from redox transitions. The following findings contribute to the further understanding and interpretation of the paleoenvironmental significance of geochemical signals in sedimentary environments associated with regional-scale deoxygenation events in deep-marine settings:

1) By analyzing the large geochemical dataset obtained from different EM locations representing diverse oceanographic regimes, it is suggested that certain trace elements such as Mo, V, U, Co, and Ni are more reliable as redox proxies compared to other redox sensitive elements such as Cr, Cu, Pb, and Zn, since they show weaker detritic influence.
2) This study demonstrates the need for a precise understanding of postdepositional processes for accurate interpretations of geochemical signals, and subsequently a robust paleoenvironmental analysis since postdepositional remobilization can produce RSTMs enrichments above and/or below the organic-rich sediments. For example, caution must be exercised when interpreting Mo signals, as it has been demonstrated that dissolved Mo to can be readily scavenged by

pyrite aggregates and Mn-oxyhydroxides during early diagenesis. Similarly, caution is necessary when considering U signals due to the potential downward migration of the syndepositional signal caused by intense bioirrigation.

3) The calibration plots and the synchronous enrichment of V, U, Mo, and other RSTMs in the vertical profiles provide support that deoxygenation in EM deep-marine settings during sapropel onsets occurred abruptly. Furthermore, the calibration plots underscore the significant influence of local environmental conditions (e.g., productivity rate) and hydrogeographic features (e.g., water-depth, sedimentation rate, and particulate-shuttling intensity) in governing the authigenic rates of RSTMs by seafloor sediments and determining the redox thresholds of geochemical proxies. In this sense, deep-marine settings characterized by intense particulate-shuttling appear to exhibit higher redox threshold values (e.g., Mediterranean Ridge), whereas deep-marine settings with weaker particulate-shuttling and more prone to abrupt and early bottom-water stagnation seem to lead to lower redox thresholds values (e.g., Ionian Basin).

Overall, these findings demonstrate that a careful consideration of postdepositional processes and local hydrogeographic factors is essential for an accurate understanding and interpretation of geochemical signals derived from regional-scale deoxygenation events in deep-marine settings. Such findings are therefore crucial in advancing our understanding of past and present deoxygenation dynamics, contributing to better forecasting and management of marine environments facing the challenge of increasing marine deoxygenation.

Declaration of Competing Interest

The authors declare that they have no known competing financial interests or personal relationships that could have appeared to influence the work reported in this paper.

Data availability

Data will be made available on request.

Acknowledgments

This study has been funded by Grants PID2019-104624RB-I00, PID2019-104625RB-100, and TED2021-131697B-C22 funded by MCIN/AEI/ 10.13039/501100011033, Grants FEDER/Junta de Andalucía P18-RT-3804 and P18-RT-4074, and by Research Groups RNM-179 and RNM-178 funded by Junta de Andalucía. We thank Prof. Adatte from Lausanne University (Switzerland) for Rock-eval analyses and TOC measurements. We are also grateful to the Center for Scientific Instrumentation (CIC, University of Granada) and the XRF Unit of the IACT (CSIC-UGR) for the ICP and XRF analyses, respectively. We are grateful to the Ocean Drilling Program for providing the analyzed samples as well as to the ODP Core Repository (Bremen, Germany) for assistance with sampling. We thank the Editor, Dr. Paul Hesse, and the two anonymous reviewers for their detailed and useful comments that significantly contributed to improve the manuscript. This study is part of R. Monedero PhD project.

Appendix A. Supplementary data

Supplementary data to this article can be found online at https://doi.org/10.1016/j.palaeo.2023.111953.

References

Algeo, T.J., Li, C., 2020. Redox classification and calibration of redox thresholds in sedimentary systems. Geochim. Cosmochim. Acta 287, 8–26. https://doi.org/10.1016/j.gca.2020.01.055.

Algeo, T.J., Liu, J., 2020. A re-assessment of elemental proxies for paleoredox analysis. Chem. Geol. 540, 119549 https://doi.org/10.1016/j.chemgeo.2020.119549.

Algeo, T.J., Lyons, T.W., 2006. Mo-TOC covariation in modern anoxic marine environments: implication for analysis of paleoredox and paleohydrographic conditions. Paleoceanography 21, PA1016. https://doi.org/10.1029/2004PA001112.

Algeo, T.J., Maynard, J.B., 2004. Trace-element behavior and redox facies in core shales of Upper Pennsylvanian Kansas-type cyclothems. Chem. Geol. 206, 289–318. https://doi.org/10.1016/j.chemgeo.2003.12.009.

Algeo, T.J., Tribovillard, N., 2009. Environmental analysis of paleoceanographic systems based on molybdenum-uranium covariation. Chem. Geol. 268, 211–225. https://doi.org/10.1016/j.chemgeo.2009.09.001.

Algeo, T., Lyons, T., Blakey, C., Over, J., 2007. Hydrographic conditions of the Devono-Carboniferous North American Seaway inferred from sedimentary Mo-TOC relationships. Palaeogeogr. Palaeoclimatol. Palaeoecol. 256, 204–230. https://doi.org/10.1016/j.palaeo.2007.02.035.

Andersen, M.B., Matthews, A., Bar-Matthews, M., Vance, D., 2020. Rapid onset of ocean anoxia shown by high U and low Mo isotope compositions of sapropel S1. Geochem. Perspect. Lett. 15, 10–14. https://doi.org/10.3929/ethz-b-000445569.

Arnaboldi, M., Meyers, P., 2007. Trace element indicators of increased primary production and decreased water-column ventilation during deposition of latest Pliocene sapropels at five locations across the Mediterranean Sea. Palaeogeogr. Palaeoclimatol. Palaeoecol. 249, 425–443. https://doi.org/10.1016/j.palaeo.2007.02.016.

Azrieli-Tal, I., Matthews, A., Bar-Matthews, M., Almogi-Labin, A., Vance, D., Archer, C., Teutsch, N., 2014. Evidence from molybdenum and iron isotopes and molybdenum–uranium covariation for sulphidic bottom waters during Eastern Mediterranean sapropel S1 formation. EPSL. 393 (2), 31–242. https://doi.org/10.1016/j.epsl.2014.02.054.

Bea, F., 1996. Residence of REE, Y, Th and U in granites and crustal protoliths: implications for the chemistry of crustal melts. J. Petrol. 37, 521–532. https://doi.org/10.1093/petrology/37.3.521.

Behar, F., Beaumont, V., Penteado, H.L. De B., 2001. Rock-Eval 6 technology: performances and developments. Oil Gas Sci. Technol. 56, 111–134. https://doi.org/10.2516/ogst:2001013.

Bektursunova, R., L'Heureux, I., 2011. A reaction-transport model of periodic precipitation of pyrite in anoxic marine sediments. Chem. Geol. 287, 158–170. https://doi.org/10.1016/j.chemgeo.2011.06.004.

Benkovitz, A., Matthews, A., Teutsch, N., Poulton, S.W., Bar-Matthews, M., Almogi-Labin, A., 2020. Tracing water column euxinia in Eastern Mediterranean Sapropels S5 and S7. Chem. Geol. 545, 119627 https://doi.org/10.1016/j.chemgeo.2020.119627.

Berner, R.A., 1969. Migration of iron and sulfur within anaerobic sediments during early diagenesis. Am. J. Sci. 267, 19–42. https://doi.org/10.2475/ajs.267.1.19.

Berner, R.A., 1970. Sedimentary pyrite formation. Am. J. Sci. 268, 1–23. https://doi.org/10.2475/ajs.268.1.1.

Berner, R.A., 1981. A new geochemical classification of sedimentary environments. J. Sediment. Res. 51, 359–365. https://doi.org/10.1306/212F7C7F-2B24-11D7-8648000102C1865D.

Berrang, P.G., Grill, E.V., 1974. The effect of manganese oxide scavenging on molybdenum in Saanich inlet, British Columbia. Mar. Chem. 2, 125–148. https://doi.org/10.1016/0304-4203(74)90033-4.

Bishop, J., 1988. The barite-opal-organic carbon association in oceanic particulate matter. Nature 332, 341–343. https://doi.org/10.1038/332341a0.

Bout-Roumazeilles, V., Combourieu-Nebout, N., Desprat, S., Siani, G., Turon, J.-L., Essallami, L., 2013. Tracking atmospheric and riverine terrigenous supplies variability during the last glacial and the Holocene in central Mediterranean. Clim. Past 9, 1065–1087. https://doi.org/10.5194/cp-9-1065-2013.

Breitburg, D., Levin, L.A., Oschlies, A., Grégoire, M., Chavez, F.P., Conley, D.J., Garçon, V., Gilbert, D., Gutiérrez, D., Isensee, K., Jacinto, G.S., Limburg, K.E., Montes, I., Naqvi, S.W.A., Pitcher, G.C., Rabalais, N.N., Roman, M.R., Rose, K.A., Seibel, B.A., Telszewski, M., Yasuhara, M., Zhang, J., 2018. Declining oxygen in the global ocean and coastal waters. Science 359, 6371. https://doi.org/10.1126/science.aam7240.

Brumsack, H.J., 2006. The trace metal content of recent organic carbon-rich sediments: Implications for cretaceous black shale formation. Palaeogeogr. Palaeoclimatol. Palaeoecol. 232, 344–361. https://doi.org/10.1016/j.palaeo.2005.05.011.

Calvert, S.E., Pedersen, T.F., 1993. Geochemistry of recent oxic and anoxic sediments: implications for the geological record. Mar. Geol. 113, 67–88. https://doi.org/10.1016/0025-3227(93)90150-T.

Calvert, S.E., Pedersen, T.F., 2007. Chapter fourteen elemental proxies for palaeoclimatic and palaeoceanographic variability in marine sediments: interpretation and application. Dev. Mar. Geol. 1, 567–644. https://doi.org/10.1016/S1572-5480(07)01019-6.

Canfield, D.E., Thamdrup, B., 2009. Towards a consistent classification scheme for geochemical environments, or, why we wish the term 'suboxic' would go away. Geobiology 4, 385–392. https://doi.org/10.1111/j.1472-4669.2009.00214.x.

Casford, J.S.L., Rohling, E.J., Abu-Zied, R.H., Jorissen, F.J., Leng, M., Thomson, J., 2003. A dynamic concept for eastern Mediterranean circulation and oxygenation during sapropel formation. Palaeogeogr. Palaeoclimatol. Palaeoecol. 190, 103–119. https://doi.org/10.1016/S0031-0182(02)00601-6.

Chang, J., Li, Y., Lu, H., 2022. The morphological characteristics of authigenic pyrite formed in marine sediments. J. Mar. Sci. Eng. 10, 1533. https://doi.org/10.3390/jmse10101533.

Cita, M.B., Grignani, D., 1982. Nature and origin of Late Neogene Mediterranean sapropels. In: Schlanger, S.O., M.B (Eds.), Nature and Origin of Cretaceous Carbon-Rich Facies. Academic, San Diego, California, USA, pp. 165–196.

Cita, M.B., Vergnaud-Grazzini, C., Robert, C., Chamley, H., Ciaranfi, N., Donofrio, S., 1977. Paleoclimatic record of a long deep-sea core from the eastern Mediterranean. Quatern. Res. 8, 205–235. https://doi.org/10.1016/0033-5894(77)90046-1.

Crusius, J., Calvert, S., Pedersen, T., Sage, D., 1996. Rhenium and molybdenum enrichments in sediments as indicators of oxic, suboxic, and sulfidic conditions of deposition. Earth Planet. Sci. Lett. 145, 65–78. https://doi.org/10.1016/S0012-821X(96)00204-X.

de Lange, G.J., 1986. Early diagenetic reactions in interbedded pelagic and turbiditic sediments in the Nares Abyssal Plain (western North Atlantic): consequences for the composition of sediment and interstitial water. Geochim. Cosmochim. Acta 50, 2543–2561. https://doi.org/10.1016/0016-7037(86)90209-7.

de Lange, G.J., Middelburg, J.J., Pruysers, P.A., 1989. Discussion: Middle and Late Quaternary depositional sequences and cycles in the eastern Mediterranean. Sedimentology 36, 151–156. https://doi.org/10.1111/j.1365-3091.1989.tb00827.x.

de Lange, G.J., Thomson, J., Reitz, A., Slomp, C.P., Speranza Principato, M., Erba, E., Corselli, C., 2008. Synchronous basin-wide formation and redox-controlled preservation of a Mediterranean sapropel. Nat. Geosci. 1, 606–610. https://doi.org/10.1038/ngeo283.

Dehairs, F., Lambert, C.E., Chesselet, R., Risler, N., 1987. The biological production of marine suspended barite and the barium cycle in the Western Mediterranean Sea. Biogeochemistry 4, 119–139. https://doi.org/10.1007/BF02180151.

Dellwig, O., Leipe, T., März, C., Glockzin, M., Pollehne, F., Schnetger, B., Yakushev, E.V., Böttcher, M.E., Brumsack, H.J., 2010. A new particulate Mn-Fe-P-shuttle at the redoxcline of anoxic basins. Geochim. Cosmochim. Acta 74, 7100–7115. https://doi.org/10.1016/j.gca.2010.09.017.

Dickson, A.J., Gill, B.C., Ruhl, M., Jenkyns, H.C., Porcelli, D., Idiz, E., Lyons, T.W., van den Boorn, S.H.J.M., 2017. Molybdenum-isotope chemostratigraphy and paleoceanography of the Toarcian Oceanic Anoxic Event (early Jurassic). Paleoceanogr. 32, 813–829. https://doi.org/10.1002/2016pa003048.

Dickson, A.J., Bagard, M.-L., Katchinoff, J.A.R., Davies, M., Poulton, S.W., Cohen, A.S., 2021. Isotopic constraints on ocean redox at the end of the Eocene. Earth Planet. Sci. Lett. 562, 116814 https://doi.org/10.1016/j.epsl.2021.116814.

Emeis, K.C., Robertson, A.H.F., Richter, C., Shipboard Scientific Party, 1996. Proc. ODP, Init. Repts, 160. Ocean Drilling Program, College Station, TX. https://doi.org/10.2973/odp.proc.ir.160.1996.

Emeis, K.C., Sakamoto, T., Wehausen, R., Brumsack, H.J., 2000. The sapropel record of the eastern Mediterranean Sea - results of Ocean Drilling Program Leg 160. Palaeogeogr. Palaeoclimatol. Palaeoecol. 158, 371–395. https://doi.org/10.1016/S0031-0182(00)00059-6.

Emeis, K.C., Schulz, H., Struck, U., Rossignol-Strick, M., Erlenkeuser, H., Howell, M.W., Kroon, D., Mackensen, A., Ishizuka, S., Oba, T., Sakamoto, T., Koizumi, I., 2003. Eastern Mediterranean surface water temperatures and delta O-18 composition during deposition of sapropels in the late Quaternary. Paleoceanography 18, 1–18. https://doi.org/10.1029/2000PA000617.

Fernández-Martínez, J., Martínez Ruíz, F., Rodríguez-Tovar, F.J., Piñuela, L., García-Ramos, J.C., Algeo, T.J., 2023. Euxinia and hydrographic restriction in the Tethys Ocean: Reassessing global oceanic anoxia during the early Toarcian. Glob. Planet. Change 221, 104026. https://doi.org/10.1016/j.gloplacha.2022.104026.

Filippidi, A., de Lange, G.J., 2019. Eastern Mediterranean deep water formation during sapropel S1: a reconstruction using geochemical records along a bathymetric transect in the Adriatic outflow region. Paleoceanogr. Paleoclimatol. 34, 409–429. https://doi.org/10.1029/2018PA003459.

Filippidi, A., Triantaphyllou, M.V., de Lange, G.J., 2016. Eastern-Mediterranean ventilation variability during sapropel S1 formation, evaluated at two sites influenced by deep-water formation from Adriatic and Aegean seas. Quat. Sci. Rev. 144, 95–106. https://doi.org/10.1016/j.quascirev.2016.05.024.

Gallego-Torres, D., Martínez-Ruiz de Lange, G., Jiménez-Espejo, F., Ortega-Huertas, M., 2007a. Trace-elemental derived paleoceanographic and paleoclimatic conditions for Pleistocene Eastern Mediterranean sapropels. Palaeogeogr. Palaeoclimatol. Palaeoecol. 293, 76–89. https://doi.org/10.1016/j.palaeo.2010.05.001.

Gallego-Torres, D., Martínez-Ruiz, F., Jiménez-Espejo, F., Ortega-Huertas, M., 2007b. Pliocene-Holocene evolution of depositional conditions in the eastern Mediterranean: Role of anoxia vs. productivity at time of sapropel deposition. Palaeogeogr. Palaeoclimatol. Palaeoecol. 246, 424–439. https://doi.org/10.1016/j.palaeo.2006.10.008.

Gallego-Torres, D., Martínez-Ruiz, F., Meyers, P., Jiménez-Espejo, F., Ortega-Huertas, M., 2010. Productivity patterns and N-fixation associated with Pliocene-Holocene sapropels: paleoceanographic and paleoecological significance. Biogeosci. Discuss. 8, 415–431. https://doi.org/10.5194/bg-8-415-2011.

Giorgi, F., 2006. Climate change hot-spots. Geophys. Res. Lett. 33, L08707. https://doi.org/10.1029/2006GL025734.

Giorgi, F., Lionello, P., 2008. Climate change projections for the Mediterranean region. Glob. Planet. Change 63, 90–104. https://doi.org/10.1016/j.gloplacha.2007.09.005.

Grant, K.M., Rohling, E.J., Ramsey, C.B., Cheng, H., Edwards, R.L., Florindo, F., Heslop, D., Marra, F., Roberts, A.P., Tamisiea, M.E., Williams, F., 2014. Sea-level variability over five glacial cycles. Nat. Commun. 5, 5076. https://doi.org/10.1038/ncomms6076.

Grant, K.M., Grimm, R., Mikolajewicz, U., Marino, G., Ziegler, M., Rohling, E.J., 2016. The timing of Mediterranean sapropel deposition relative to insolation, sea-level and African monsoon changes. Quat. Sci. Rev. 140, 125–141. https://doi.org/10.1016/j.quascirev.2016.03.026.

Grema, H.M., Magnall, J.M., Whitehouse, M.J., Gleeson, S.A., Schulz, H.M., 2022. The formation of highly positive $\delta^{34}S$ values in Late Devonian mudstones: microscale analysis of pyrite ($\delta^{34}S$) and barite ($\delta^{34}S$, $\delta^{18}O$) in the Canol Formation (Selwyn Basin, Canada). Front. Earth Sci. 9, 784824 https://doi.org/10.3389/feart.2021.784824.

Grundl, T., Haderlein, S., Nurmi, J., Tratnyek, P., 2011. Introduction to aquatic redox chemistry. In: ACS Symp. Ser. Am. Chem. Soc, 1071, pp. 1–14. https://doi.org/10.1021/bk-2011-1071.ch001.

Hammer, Ø., Harper, D.A.T., Ryan, P.D., 2001. PAST: paleontological statistics software package for education and data analysis. Palaeontol. Electron. 4, 1–9.

Helz, G.R., Miller, C.V., Charnock, J.M., Mosselmans, J.F.W., Pattrick, R.A.D., Garner, C. D., Vaughan, D.J., 1996. Mechanism of molybdenum removal from the sea and its concentration in black shales: EXAFS evidence. Geochim. Cosmochim. Acta 60, 3631–3642. https://doi.org/10.1016/0016-7037(96)00195-0.

Henkel, S., Mogollón, J.M., Nöthen, K., Franke, C., Bogus, K., Robin, E., Bahr, A., Blumenberg, M., Pape, T., Seifert, R., März, C., de Lange, G., Kasten, S., 2012. Diagenetic barium cycling in Black Sea sediments -a case study for anoxic marine environments. Geochim. Cosmochim. Acta 88, 88–105. https://doi.org/10.1016/j.gca.2012.04.021.

Hennekam, R., Jilbert, T., Schnetger, B., de Lange, G.J., 2014. Solar forcing of Nile discharge and sapropel S1 formation in the early to middle Holocene eastern Mediterranean. Paleoceanography 29, 343–356. https://doi.org/10.1002/2013PA002553.

Hennekam, R., van der Bolt, B., van Nes, E.H., de Lange, G.J., Scheffer, M., Reichart, G.J., 2020. Early-warning signals for marine anoxic events. Geophys. Res. Lett. 47 https://doi.org/10.1029/2020GL089183.

Hetzel, A., Böttcher, M.E., Wortmann, U.G., Brumsack, H.J., 2009. Paleo-redox conditions during OAE 2 reflected in Demerara rise sediment geochemistry (ODP Leg 207). Palaeogeogr. Palaeoclimatol. Palaeoecol. 273, 302–328. https://doi.org/10.1016/j.palaeo.2008.11.005.

Higgs, N.C., Thomson, J., Wilson, T.R.S., Croudace, I.W., 1994. Modification and complete removal of eastern Mediterranean sapropels by postdepositional oxidation. Geology 22, 423–426. https://doi.org/10.1130/0091-7613(1994)022<0423:MACROE>2.3.CO;2.

Jacobs, L., Emerson, S., Skei, J., 1985. Partitioning and transport of metals across the O2/H2S interface in a permanently anoxic basin: Framvaren Fjord, Norway. Geochim. Cosmochim. Acta 49, 1433–1444. https://doi.org/10.1016/0016-7037(85)90293-5.

Jenkyns, H.C., 1985. The early Toarcian and Cenomanian-Turonian anoxic events in Europe: comparisons and contrasts. Geol. Rundsch. 74, 505–518. https://doi.org/10.1007/bf01821208.

Jilbert, T., Reichart, G.J., Mason, P., de Lange, G.J., 2010. Short-time-scale variability in ventilation and export productivity during the formation of Mediterranean sapropel S1. Paleoceanography 25, PA4232. https://doi.org/10.1029/2010PA001955.

Keeling, R.A., Körtzinger, A., Gruber, N., 2010. Ocean deoxygenation in a warming world. Ann. Rev. Mar. Sci. 2, 199–229. https://doi.org/10.1146/annurev.marine.010908.163855.

Kidd, R.B., Cita, M.B., Ryan, W.B.F., 1978. Stratigraphy of eastern Mediterranean sapropel sequences recovered during Leg 42A and their paleoenvironmental significance. Initial Rep. Deep Sea Drill. Proj. 42A, 421–443. https://doi.org/10.2973/dsdp.proc.42-1.113-1.1978.

Lafargue, E., Marquis, F., Pillot, D., 1998. Rock-Eval 6 applications in hydrocarbon exploration, production, and soil contamination studies. Oil Gas Sci. Technol. 53, 421–437. https://doi.org/10.2516/ogst:1998036.

Lascaratos, A., Roether, W., Nittis, K., Klein, B., 1999. Recent changes in deep water formation and spreading in the eastern Mediterranean Sea: a review. Prog. Oceanogr. 44, 5–36. https://doi.org/10.1016/S0079-6611(99)00019-1.

Laskar, J., Joutel, F., Boudin, F., 1993. Orbital, precessional, and insolation quantities for the Earth from − 20 Myr to + 10 Myr. Astron. Astrophys. 270, 522–533.

Levin, L.A., 2018. Manifestation, drivers, and emergence of open ocean deoxygenation. Ann. Rev. Mar. Sci. 10, 229–260. https://doi.org/10.1146/annurev-marine-121916-063359.

Light, T., Garcia, M., Prairie, J.C., Martínez-Ruiz, F., Norris, R., 2023. Water column barium sulfate dissolution and shielding by organic matter aggregates: implications for the pelagic barite proxy. Chem. Geol. 121637 https://doi.org/10.1016/j.chemgeo.2023.121637.

Lin, Q., Wang, J., Algeo, T.J., Sun, F., Lin, R., 2016. Enhanced framboidal pyrite formation related to anaerobic oxidation of methane in the sulfate-methane transition zone of the northern South China Sea. Mar. Geol 379, 100–108. https://doi.org/10.1016/j.margeo.2016.05.016.

Lionello, P., Malanotte-Rizzoli, P., Boscolo, R., Alpert, P., Artale, V., Li, L., Luterbacher, J., May, W., Trigo, R., Tsimplis, M., Ulbrich, U., Xoplaki, E., 2006. The Mediterranean climate: an overview of the main characteristics and issues. Dev. Earth Environ. Sci. 4, 1–26. https://doi.org/10.1016/S1571-9197(06)80003-0.

Little, S.H., Vance, D., Lyons, T.W., McManus, J., 2015. Controls on trace metal authigenic enrichment in reducing sediments: insights from modern oxygen-deficient settings. Am. J. Sci. 315, 77–119. https://doi.org/10.2475/02.2015.01.

Liu, Z., Chen, D., Zhang, J., Lü, X., Wang, Z., Liao, W., Shi, X., Tang, J., Xie, G., 2019. Pyrite morphology as an indicator of paleoredox conditions and shale gas content of the Longmaxi and Wufeng Shales in the middle Yangtze Area, South China. Minerals 9, 428. https://doi.org/10.3390/min9070428.

Lourens, L.J., Antonarakou, A., Hilgen, F.J., Van Hoof, A.A.M., Vergnaud-Grazzini, C., Zachariasse, W.J., 1996. Evaluation of the Plio-Pleistocene astronomical time-scale. Paleoceanography 11, 391–413. https://doi.org/10.1029/96PA01125.

Löwemark, L., Lin, Y., Chin, H.F., Yang, T.N., Beier, C., Werner, F., Lee, C.Y., Song, S.R., Kao, S.J., 2006. Sapropel burn-down and ichnological response to late Quaternary sapropel formation in two ~ 400 ky records from the eastern Mediterranean Sea. Palaeogeogr. Palaeoclimatol. Palaeoecol. 239, 406–425. https://doi.org/10.1016/j.palaeo.2006.02.013.

Lyons, T.W., Anbar, A.D., Severmann, S., Scott, C., Gill, B.C., 2009. Tracking euxinia in the ancient ocean: a multiproxy perspective and Proterozoic case study. Annu. Rev. Earth Planet. Sci. 37, 507–534. https://doi.org/10.1146/annurev.earth.36.031207.124233.

Mancini, A.M., Bocci, G., Morigi, C., Gennari, R., Lozar, F., Negri, A., 2023. Past analogues of deoxygenation events in the Mediterranean Sea: a tool to constrain future impacts. J. Mar. Sci. Eng. 11, 562. https://doi.org/10.3390/jmse11030562.

Martínez-Ruiz, F., Kastner, M., Paytan, A., Ortega-Huertas, M., Bernasconi, S.M., 2000. Geochemical evidence for enhanced productivity during S1 sapropel deposition in the eastern Mediterranean. Paleoceanography 15, 200–209. https://doi.org/10.1029/1999PA000419.

Marino, G., Rohling, E.J., Sagiorgi, F., Sinninghe, D.J., Hayes, A., Casford, J.L., Lotter, A. F., Kucera, M., Brinkhuis, H., 2009. Early and middle Holocene in the Aegean Sea: interplay between high and low latitude climate variability. Quat. Sci. Rev. 28, 3246–3262. https://doi.org/10.1016/j.quascirev.2009.08.011.

Martínez-Ruiz, F., Jroundi, F., Paytan, A., Guerra-Tschuschke, I., Abad, M.M., González-Muñoz, M.T., 2018. Barium bioaccumulation by bacterial biofilms and implications for Ba cycling and use of Ba proxies. Nat. Commun. 9, 1619. https://doi.org/10.1038/s41467-018-04069-z.

Martínez-Ruiz, F., Paytan, A., Gonzalez-Muñoz, M.T., Jroundi, F., Abad, M.M., Lam, P., Bishop, J.K.B., Horner, T.J., Morton, P., Kastner, M., 2019. Barite formation in the ocean: origin of amorphous and crystalline precipitates. Chem. Geol. 511, 441–451. https://doi.org/10.1016/j.chemgeo.2018.09.011.

Martínez-Ruiz, F., Paytan, A., Gonzalez-Muñoz, M.T., Jroundi, F., Abad, M.M., Lam, P.J., Horner, T.J., Kastner, M., 2020. Barite precipitation on suspended organic matter in the Mesopelagic Zone. Front. Earth Sci. 8, 567714 https://doi.org/10.3389/feart.2020.567714.

McArthur, J., 2019. Early Toarcian black shales: a response to an oceanic anoxic event or anoxia in marginal basins? Chem. Geol. 522, 71–83. https://doi.org/10.1016/j.chemgeo.2019.05.028.

McManus, J., Berelson, W.M., Klinkhammer, G.P., Kilgore, T.E., Hammond, D.E., 1994. Remobilization of barium in continental margin sediments. Geochim. Cosmochim. Acta 58, 4899–4907. https://doi.org/10.1016/0016-7037(94)90220-8.

McManus, J., Berelson, W.M., Klinkhammer, G.P., Johnson, K.S., Coale, K.H., Anderson, R.F., Kumar, N., Burdige, D.J., Hammond, D.E., Brumsack, H.J., McCorkle, D.C., Rushdi, A., 1998. Geochemistry of barium in marine sediments: implications for its use as a paleoproxy. Geochim. Cosmochim. Acta 62, 21–22. https://doi.org/10.1016/S0016-7037(98)00248-8.

McManus, J., Berelson, W.M., Klinkhammer, G.P., Hammond, D.E., Holm, C., 2005. Authigenic uranium: relationship to oxygen penetration depth and organic carbon rain. Geochim. Cosmochim. Acta 69, 95–108. https://doi.org/10.1016/j.gca.2004.06.023.

Merinero, R., Cardenes, V., Lunar, R., Boone, M., Cnudde, V., 2017. Representative size distributions of framboidal, euhedral and sunflower pyrite from high-resolution X-ray tomography and scanning electron microscopy analyses. Am. Mineral. 102, 620–631. https://doi.org/10.2138/am-2017-5851.

Miller, A.R., 1963. Physical Oceanography of the Mediterranean Sea: a discourse. Rapp. Comm. Int. Mer Médit. 17, 857–887.

Millot, C., 1999. Circulation in the Western Mediterranean Sea. J. Mar. Syst. 20, 423–442. https://doi.org/10.1016/S0924-7963(98)00078-5.

Millot, C., 2009. Another description of the Mediterranean Sea outflow. Prog. Oceanogr. 82, 101–124. https://doi.org/10.1016/j.pocean.2009.04.016.

Millot, C., Taupier-Letage, I., 2005. Circulation in the Mediterranean Sea. In: Saliot, A. (Ed.), The Mediterranean Sea, Handb. Environ. Chem, 5. Springer, Berlin, Heidelberg, pp. 26–66. https://doi.org/10.1007/b107143.

Monedero-Contreras, R.D., Martínez-Ruiz, F., Rodríguez-Tovar, F.J., 2023a. Role of climate variability on deep-water dynamics and deoxygenation during sapropel deposition: new insights from a palaeoceanographic empirical approach. Palaeogeogr. Palaeoclimatol. Palaeoecol. 622, 111601 https://doi.org/10.1016/j.palaeo.2023.111601.

Monedero-Contreras, R.D., Martínez-Ruiz, F., Rodríguez-Tovar, F.J., 2023b. Evidence of postdepositional remobilization of redox-sensitive metals across sapropel boundaries: new insights from LA-ICP-MS and EDX mapping analyses. Chem. Geol. 121643 https://doi.org/10.1016/j.chemgeo.2023.121643.

Morford, J.L., Emerson, S.R., Breckel, E.J., Kim, S.H., 2005. Diagenesis of oxyanions (V, U, Re, and Mo) in pore waters and sediments from a continental margin. Geochim. Cosmochim. Acta 69, 5021–5032. https://doi.org/10.1016/j.gca.2005.05.015.

Murat, A., Got, H., 1987. Middle and Late Quaternary depositional sequences and cycles in the eastern Mediterranean. Sedimentology 34, 885–889. https://doi.org/10.1111/j.1365-3091.1987.tb00810.x.

Nijenhuis, I.A., Bosch, H.J., Damsté, J.S., Brumsack, H.J., de Lange, G.J., 1999. Organic matter and trace element rich sapropels and black shales: a geochemical comparison. Earth Planet. Sci. Lett. 169, 277–290. https://doi.org/10.1016/S0012-821X(99)00083-7.

Ordoñez, L., Vogel, H., Sebag, D., Ariztegui, D., Adatte, T., Russell, J.M., Kallmeyer, J., Vuillemin, A., Friese, A., Crowe, S.A., Bauer, K.W., Simister, R., Henny, C., Nomosatryo, S., Bijaksana, S., 2019. Empowering conventional Rock-Eval pyrolysis for organic matter characterization of the siderite-rich sediments of Lake Towuti (Indonesia) using End-Member Analysis. Org. Geochem. 134, 32–44. https://doi.org/10.1016/j.orggeochem.2019.05.002.

Passier, H.F., Middelburg, J.J., van Os, B.J.H., de Lange, G.J., 1996. Diagenetic pyritisation under eastern Mediterranean sapropels caused by downward sulphide diffusion. Geochim. Cosmochim. Acta 60, 751–776. https://doi.org/10.1016/0016-7037(95)00419-X.

Passier, H.F., Middelburg, J., de Lange, G., Böttcher, M., 1997. Pyrite contents, microtextures, and sulfur isotopes in relation to formation of the youngest eastern Mediterranean sapropel. Geology 25, 519–522. https://doi.org/10.1130/0091-7613(1997)025<0519:PCMASI>2.3.CO;2.

Passier, H.F., Bosch, H.J., Nijenhuis, I., Lourens, L., Böttcher, M., Leenders, A., Sinninghe-Damste, J., de Lange, G., de Leeuw, J., 1999. Sulphic Mediterranean surface waters during Pliocene sapropel formation. Nature 397, 146–149. https://doi.org/10.1038/16441.

Paul, K.M., van Heldmond, N.A.G.M., Slomp, C.P., Jokinen, S.A., Virtasalo, J.J., Filipsson, H.L., Jilbert, T., 2023. Sedimentary molybdenum and uranium: improving proxies for deoxygenation in coastal depositional environments. Chem. Geol. 615, 121203 https://doi.org/10.1016/j.chemgeo.2022.121203.

Paytan, A., Griffith, E.M., 2007. Marine barite: recorder of variations in ocean export productivity. Deep Sea Res. Part Topical Stud. Oceanogr. 54, 687–705.

Paytan, A., Mearon, S., Cobb, K., Kastner, M., 2002. Origin of marine barite deposits: Sr and S isotope characterization. Geol 30, 747–750.

Paytan, A., Martínez-Ruiz, F., Eagle, M., Ivy, A., Wankel, S., 2004. Using sulfur isotopes to elucidate the origin of barite associated with high organic matter accumulation events in marine sediments. Geol. Soc. Am. Spec. Paper 379, 151–160.

Pinardi, N., Masetti, E., 2000. Variability of the large scale general circulation of the Mediterranean Sea from observations and modelling: a review. Palaeogeogr. Palaeoclimatol. Palaeoecol. 158, 153–173. https://doi.org/10.1016/S0031-0182(00)00048-1.

Pinardi, N., Zavatarelli, M., Adani, M., Coppini, G., Fratianni, C., Oddo, P., Simoncelli, S., Tonani, M., Lyubartsev, V., Dobricic, S., Bonaduce, A., 2015. Mediterranean Sea large-scale low-frequency ocean variability and water mass formation rates from 1987 to 2007: a retrospective analysis. Progress. Oceanogr. 132, 318–332. https://doi.org/10.1016/j.pocean.2013.11.003.

Pruysers, P.A., de Lange, G.J., Middelburg, J.J., 1991. Geochemistry of eastern Mediterranean sediments: primary sediment composition and diagenetic alterations. Mar. Geol. 100, 137–154. https://doi.org/10.1016/0025-3227(91)90230-2.

Pruysers, P.A., de Lange, G.J., Middelburg, J.J., Hydes, D.J., 1993. The diagenetic formation of metal-rich layers in sapropel-containing sediments in the eastern Mediterranean. Geochim. Cosmochim. Acta 57, 527–536. https://doi.org/10.1016/0016-7037(93)90365-4.

Reershemius, T., Planavsky, N.J., 2021. What controls the duration and intensity of ocean anoxic events in the Paleozoic and the Mesozoic? Earth Sci. Rev. 221, 103787 https://doi.org/10.1016/j.earscirev.2021.103787.

Reitz, A., Thomson, J., de Lange, G.J., Hensen, C., 2006. Source and development of large manganese enrichments above eastern Mediterranean sapropel S1. Paleoceanography 21, PA3007. https://doi.org/10.1029/2005PA001169.

Rohling, E.J., Marino, G., Grant, K.M., 2015. Mediterranean climate and oceanography, and the periodic development of anoxic events (sapropels). Earth Sci. Rev. 143, 62–97. https://doi.org/10.1016/j.earscirev.2015.01.008.

Rossignol-Strick, M., 1983. African monsoons, an immediate climate response to orbital insolation. Nature 304, 46–49. https://doi.org/10.1038/304046a0.

Rossignol-Strick, M., 1985. Mediterranean Quaternary sapropels, an immediate response of the African monsoon to variation of insolation. Palaeogeogr. Palaeoclimatol. Palaeoecol. 49, 237–263. https://doi.org/10.1016/0031-0182(85)90056-2.

Scheiderich, K., Zerkl, A.L., Helz, G.R., Farquhar, J., Walker, R.J., 2010. Molybdenum isotope, multiple sulfur isotope, and redox-sensitive element behavior in early. Pleistocene Mediterranean sapropels. Chem. Geol. 279, 134–144. https://doi.org/10.1016/j.chemgeo.2010.10.015.

Schmidtko, S., Stramma, L., Visbeck, M., 2017. Decline in global oceanic oxygen content during the past five decades. Nature 542, 335–339. https://doi.org/10.1038/nature21399.

Scholz, F., 2018. Identifying oxygen minimum zone-type biogeochemical cycling in Earth history using inorganic geochemical proxies. Earth Sci. Rev. 184, 29–45. https://doi.org/10.1016/j.earscirev.2018.08.002.

Scholz, F., McManus, J., Sommer, S., 2013. The manganese and iron shuttle in a modern euxinic basin and implications for molybdenum cycling at euxinic ocean margins. Chem. Geol. 355, 56–68. https://doi.org/10.1016/j.chemgeo.2013.07.006.

Scholz, F., Siebert, C., Dale, A.W., Frank, M., 2017. Intense molybdenum accumulation in sediments underneath a nitrogenous water column and implications for the reconstruction of paleo-redox conditions based on molybdenum isotopes. Geochim. Cosmochim. Acta 213, 400–417. https://doi.org/10.1016/j.gca.2017.06.048.

Schulte, P., Schwark, L., Stassen, P., Kouwenhoven, T.J., Bornemann, A., Speijer, R.P., 2013. Black shale formation during the Latest Danian Event and the Paleocene–Eocene Thermal Maximum in central Egypt: Two of a kind? Palaeogeogr. Palaeoclimatol. Palaeoecol. 371, 9–25. https://doi.org/10.1016/j.palaeo.2012.11.027.

Scott, C., Lyons, T.W., 2012. Contrasting molybdenum cycling and isotopic properties in euxinic versus non-euxinic sediments and sedimentary rocks: refining the paleoproxies. Chem. Geol. 324-325, 19–27. https://doi.org/10.1016/j.chemgeo.2012.05.012.

Sweere, S., van den Boorn, S., Dickson, A.J., Reichart, G.J., 2016. Definition of new trace-metal proxies for the controls on organic matter enrichment in marine sediments based on Mn, Co, Mo and Cd concentrations. Chem. Geol. 441, 235–245. https://doi.org/10.1016/j.chemgeo.2016.08.028.

Sweere, T., Hennekam, R., Vance, D., Reichart, G.J., 2021. Molybdenum isotope constraints on the temporal development of sulfidic conditions during

Mediterranean sapropel intervals. Geochem. Persp. Lett. 17, 16–20. https://doi.org/10.7185/geochemlet.2108.
Tachikawa, K., Vidal, L., Cornuault, M., Garcia, M., Pothin, A., Sonzogni, C., Bard, E., Ménot, G., Revel, M., 2015. Eastern Mediterranean Sea circulation inferred from the conditions of S1 sapropel deposition. Clim. Past 11, 855–867. https://doi.org/10.5194/cp-11-855-2015.
Taylor, S.R., McLennan, S.M., 1995. The geochemical evolution of the continental crust. Rev. Geophys. 33, 241–265. https://doi.org/10.1029/95RG00262.
Tesi, T., Asioli, A., Minisini, D., Maselli, V., Dalla Valle, G., Gamberi, F., Langone, L., Cattaneo, A., Montagna, P., Trincardi, F., 2017. Large-scale response of the Eastern Mediterranean thermohaline circulation to African monsoon intensification during sapropel S1 formation. Quat. Sci. Rev. 159, 139–154. https://doi.org/10.1016/j.quascirev.2017.01.020.
Thomson, J., Higgs, N.C., Croudace, I.W., Colley, S., Hydes, D.J., 1993. Redox zonation of elements at an oxic/post-oxic boundary in deep-sea sediments. Geochim. Cosmochim. Acta 57, 579–595. https://doi.org/10.1016/0016-7037(93)90369-8.
Thomson, J., Higgs, N.C., Wilson, T.R.S., Croudace, I.W., de Lange, G.J., van Santvoort, J. M., 1995. Redistribution and geochemical behavior of redox-sensitive elements around S1, the most recent easter Mediterranean sapropel. Geochim. Cosmochim. Acta 59, 3487–3501. https://doi.org/10.1016/0016-7037(95)00232-O.
Thomson, J., Mercone, D., de Lange, G.J., van Santvoort, J.M., 1999. Review of recent advances in the interpretation of eastern Mediterranean sapropel SI from geochemical evidence. Mar. Geol. 153, 77–89.
Torres, M.E., Brumsack, H.j., Bohrmann, G., Emeis, K.C., 1996. Barite fronts in continental margin sediments: a new look at barium remobilization in the zone of sulfate reduction and formation of heavy barites in diagenetic fronts. Chem. Geol. 127, 125–139. https://doi.org/10.1016/0009-2541(95)00090-9.
Tribovillard, N., 2021. Re-assessing copper and nickel enrichments as paleo-productivity proxies. BSGF - Earth Sci. Bull. 192, 54. https://doi.org/10.1051/bsgf/2021047.
Tribovillard, N., Algeo, T.J., Lyons, T., Riboulleau, A., 2006. Trace metals as paleoredox and paleoproductivity proxies: an update. Chem. Geol. 232, 12–32. https://doi.org/10.1016/j.chemgeo.2006.02.012.
Tribovillard, N., Lyons, T.W., Riboulleau, A., Bout-Roumazeilles, V., 2008. A possible capture of molybdenum during early diagenesis of dysoxic sediments. Bull. Soc. Geol. Fr. 179, 3–12. https://doi.org/10.2113/gssgfbull.179.1.3.
Tribovillard, N., Algeo, T.J., Baudin, F., Riboulleau, A., 2012. Analysis of marine environmental conditions based onmolybdenum-uranium covariation applications to Mesozoic paleoceanography. Chem. Geol. 325, 46–58. https://doi.org/10.1016/j.chemgeo.2011.09.009.
Turco, M., Palazzi, E., Von Hardenberg, J., Provenzale, A., 2015. Observed climate change hotspots. Geophys. Res. Lett. 42, 3521–3528. https://doi.org/10.1002/2015GL063891.
Tyson, R., Pearson, T., 1991. Modern and ancient continental shelf anoxia: an overview. Geol. Soc. Spec. Publ. 58, 1–24. https://doi.org/10.1144/GSL.SP.1991.058.01.01.
van Os, B.J.H., 1993. Primary diagenesis signals in Mediterranean sapropels and North Atlantic turbidities. Geo. Ultraiectina 109, 1–127.
van Os, B.J.H., Middelburg, J.J., 1991. Possible diagenetic mobilization of barium in sapropelic sediment from the eastern Mediterranean. Mar. Geol. 100, 125–136. https://doi.org/10.1016/0025-3227(91)90229-W.
van Santvoort, P.J.M., de Lange, G.J., Thomson, J., Cussen, H., Wilson, T.R.S., Krom, M. D., Strohle, K., 1996. Active post-depositional oxidation of the most recent sapropel (S1) in the eastern Mediterranean. Geochim. Cosmochim. Acta 60, 4007–4024. https://doi.org/10.1016/S0016-7037(96)00253-0.
van Santvoort, P.J.M., de Lange, G.J., Langereis, C.G., Dekkers, M.J., Paterne, M., 1997. Geochemical and Paleomagnetic evidence for the occurrence of "missing" sapropels in eastern Mediterranean sediments. Paleoceanography 12, 773–786. https://doi.org/10.1029/97PA01351.
Warning, B., Brumsack, H.J., 2000. Trace metal signatures of eastern Mediterranean sapropels. Paleogeogr. Paleoclimatol. Paleoecol. 158, 293–309. https://doi.org/10.1016/S0031-0182(00)00055-9.
Wehausen, R., Brumsack, H.-J., 2000. Chemical cycles in Pliocene sapropel-bearing and sapropel-barren eastern Mediterranean sediments. Paleogeogr. Paleoclimatol. Paleoecol. 158, 325–352. https://doi.org/10.1016/S0031-0182(00)00057-2.
Weldeab, S., Menke, V., Schmiedl, G., 2014. The pace of East African monsoon evolution during the Holocene. Geophys. Res. Lett. 41, 1724–1731. https://doi.org/10.1002/2014GL059361.
Wilson, T.R.S., Thomson, J., Hydes, D.J., Colley, S., Culkin, E., Sorensen, J., 1986. Oxidation fronts in pelagic sediments: Diagenetic formation of metal-rich layers. Science 232, 972–975. https://doi.org/10.1126/science.232.4753.972.
Wu, J., Böning, P., Pahnke, K., Tachikawa, K., de Lange, G., 2016. Unraveling North-African riverine and eolian contributions to Central Mediterranean sediments during Holocene sapropel S1 formation. Quat. Sci. Rev. 152, 31–48. https://doi.org/10.1016/j.quascirev.2016.09.029.
Wu, J., Fillipidi, A., Davies, G.R., de Lange, G., 2018. Riverine supply to the eastern Mediterranean during last interglacial sapropel S5 formation: a basin-wide perspective. Chem. Geol. 485, 74–89. https://doi.org/10.1016/j.chemgeo.2018.03.037.
Wüst, G., 1961. On the vertical circulation of the Mediterranean Sea. J. Geophys. Res. 66, 3261–3271. https://doi.org/10.1029/JZ066i010p03261.
Zhang, M., Konishi, H., Xu, H., Sun, X., Lu, H., Wu, D., Wu, N., 2014. Morphology and formation mechanism of pyrite induced by the anaerobic oxidation of methane from the continental slope of the NE South China Sea. J. Asian Earth Sci. 92, 293–301. https://doi.org/10.1016/j.jseaes.2014.05.004.
Zheng, Y., Anderson, R.F., van Geen, A., Kuwabara, J., 2000. Authigenic molybdenium formation in marine sediments: a link to pore water sulfide in the Santa Barbara Basin. Geochim. Cosmochim. Acta 64, 4165–4178. https://doi.org/10.1016/S0016-7037(00)00495-6.
Zheng, Y., Anderson, R.F., van Geen, A., Fleisher, M.Q., 2002. Preservation of particulate non-lithogenic uranium in marine sediments. Geochim. Cosmochim. Acta 66, 3085–3092. https://doi.org/10.1016/S0016-7037(01)00632-9.
Ziegler, M., Tuenter, E., Lourens, L.J., 2010. The precession phase of the boreal summer monsoon as viewed from the eastern Mediterranean (ODP Site 968). Quat. Sci. Rev. 29, 1481–1490. https://doi.org/10.1016/j.quascirev.2010.03.011.
Zirks, E., Krom, M.D., Zhu, D., Schmiedl, G., Goodman-Tchernov, B.N., 2019. ACS Earth Space Chem. 3, 2287–2297. https://doi.org/10.1021/acsearthspacechem.9b00128.
Zirks, E., Krom, M., Schmiedl, G., Katz, T., Xiong, Y., Alcott, L.J., Poulton, S.W., Goodman-Tchernov, B., 2021. Redox evolution and the development of oxygen minimum zones in the Eastern Mediterranean Levantine basin during the early Holocene. Geochim. Cosmochim. Acta 297, 82–100. https://doi.org/10.1016/j.gca.2021.01.009.